Inorganic Chemistry Communications 174 (2025) 114078

Contents lists available at ScienceDirect

Inorganic Chemistry Communications

journal homepage: www.elsevier.com/locate/inoche

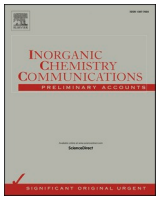

Research Article

Synthesis and optimization of TiO_2-biochar composite for degradation of Basic Blue 41 dye in textile wastewater using response surface methodology

Mohammednur Abdu [a], Saeideh Babaee [b], Abebe Worku [a], Palesa Diale [b], Titus A.M. Msagati [c], Jemal Fito Nure [b,*]

[a] Addis Ababa Science and Technology University, College of Engineering, Department of Environmental Engineering, Addis Ababa, Ethiopia
[b] School of Chemical and Metallurgical Engineering, University of the Witwatersrand, 1 Jorissen St, Johannesburg 2000, South Africa
[c] Institute for Nanotechnology and Water Sustainability (iNanoWS), College of Science, Engineering, and Technology, University of South Africa, Florida Science Campus, Johannesburg 1710, South Africa

ARTICLE INFO

Keywords:
Dyes
Effluent remediation
Micropollutant
Photodegradation
Uv-irradiation
Water pollution

ABSTRACT

This study aimed to degrade mainly Basic Blue 41 dye from textile wastewater using photocatalytic TiO_2-biochar (TiO_2-BC) composite under UV irradiation. The physicochemical characteristics of textile wastewater were examined. The TiO_2-BC was synthesized by a Sol-gel method and was characterized by Fourier-transform infrared spectroscopy (FT-IR), BET surface area analyzer, X-ray diffraction (XRD), Scanning electron microscopy- energy dispersive X-ray spectroscopy (SEM-EDS) and Raman spectroscopy. The photocatalytic performance of the TiO_2-BC composite was optimized using solution photocatalyst dosage 0.5–2.5 g/L, dye concentration 10–50 mg/L, pH 3–11, and Uv-irradiation time 30–150 min under Response Surface Methodology-Central composite design approach. The textile wastewater was characterized using temperature 45 °C, pH 5.61, electrical conductivity 1605 μS/cm, turbidity 48.5 ± 0.4 NTU, TDS 1105 mg/L, BOD_5 350 mg/L, and COD 928 mg/L. The maximum photodegradation efficiency of 99.6 % was found for the removal of BB41 dye at optimal experimental conditions of pH 8.3, initial dye concentration 40 mg/L, photocatalyst dosage 1.85 g/L, and Uv irradiation 117 min. Similarly, this photocatalytic material was also applied from remediation of the textile wastewater which resulted in the removal of BB41 dye 94.8 %, color 96.2 %, turbidity 89.3 %, and COD 66.6 %. This photodegradation process obeys the first-order kinetic model ($k = 0.049\ min^{-1}$). Finally, after over five recycling of the photocatalyst material, only a 3.3 % decrease in photodegradation efficiency was found. In conclusion, the TiO_2-BC composite material is promising and can be applied for industrial wastewater treatment at a large scale.

1. Introduction

Industrialization has spurred substantial technological progress and economic growth. However, it has also resulted in environmental degradation. The combustion of fossil fuels, the release of harmful chemicals and pollutants into the air and water, and the destruction of natural habitats have all contributed to environmental pollution [1]. Water pollution is one of the main global issues that has been growing around the world and affecting billions of people's economic growth and their environment [2,3]. The problem of water scarcity is not only associated with the available water resources but also the degradation of the existing water quality [4]. Industrial facilities have a great contribution to water pollution which releases hazardous substances to both human beings and the environment [5]. Among these industries, the textile industry ranks as the biggest user of freshwater and the foremost cause of water quality degradation. Discharging a large volume of pollutants, including dyes, metals, organic matter, and other harmful substances [6,7]. Dyes and pigments have widely been used to color different products in many sectors including textile and leather, cosmetics, and the food industry [8]. The textile industry is one of the largest consumers of various synthetic dyes [9]. Among them, azo dyes are of special significance as they constitute 70 % of the textile dyes application and produce more than half of the dyes produced globally. There are currently over 2,000 different types of azo dyes used [10,11]. During dyeing, 10–15 % of dyes are directly released into the aqueous environment which leads to severe environmental pollution. Dye in

* Corresponding author.
E-mail address: jemalfito2@gmail.com (J.F. Nure).

https://doi.org/10.1016/j.inoche.2025.114078
Received 8 October 2024; Received in revised form 23 January 2025; Accepted 7 February 2025
Available online 12 February 2025

water no matter how little can have adverse effects on the health of consumers and can lead to allergies, dermatitis, skin irritation, and cancers [12]. Basic blue 41 (BB41) dye is a cationic dye azo dye that is widely used in the textile and tannery industry for dyeing a wide range of fabrics such as polyester, cotton, viscose, wool, nylon, and silk [13]. It is also credited for contributing to serious harm to the environment because of its deep color and slow biodegradation rate [13]. The dye is widely employed in the textile sector substantially across the developing world even with a full understanding of the risks involved. Many of these dyes are released directly into water bodies without adequate treatment, they become a great risk both to the environment and people's health [14]. Efficient methods of removing BB41 dye from wastewater discharges are fundamental to prevent extra pollution and potential adverse impacts on humans and the surroundings.

Several methods have been applied for the treatment of different dyeing effluents: biological treatment; chemical oxidation; coagulation; flocculation; adsorption; membrane treatment; and advanced oxidation process (AOPs) [15]. Since the dye is complex in structure, current treatment methods for dyeing wastewater are not very effective as well as the formation of secondary pollution [16]. Among the newly developed AOPs such as Ozonation, Fenton, photo-Fenton, photolysis, and photocatalysis some are vital and cannot go through any substitution with the conventional method. Those methods effectively degraded organic molecules such as dyeing effluent, with minimal harm to the environment, and without causing secondary pollution [17]). Thus, they can be applied alone, or they can be combined with other wastewater technologies to remove the high concentration of dyes from industrial effluent. Moreover, heterogeneous photocatalysts are among the promising options of AOPs for the destruction of many recalcitrant organic pollutants. These catalysts are cost-effective, non-toxic, and offer good biological and chemical stability [18,19]. Semiconductors utilized in this category include TiO_2, ZnO, CeO_2, WO_3, SnO_2, ZrO_2, CdS and ZnS [20]. TiO_2 is a widely used photocatalyst, due to its good catalytic performance, cost-effectiveness, abundance, high chemical stability, non-toxic nature, biological inertness, and reusability [21,22]. However, its wide bandgap (3.0–3.2 eV) restricts it to use in UV light areas which accounts for only 5 % of the sun light; additionally, its recycling aspect is still an issue [12,17]. To overcome these challenges, modifications like metal doping (Fe, Se, Cr) [23], non-metal doping (B, N, P) [3], and compositing with other materials like ZnO and WO3 [24], have been made. However, metal doping brought about environmental issues like metal leaching, high expense, and low life expectancy [25,26], while non-metal doping endangered building up of defects and low stability [3,27]. These limitations have contributed to the emergence of TiO_2-adsorbent composites as viable options to replace traditional adsorbents. Integration of TiO_2 with carbon-based composites has been considered due to its high adsorption capacity and improvement of photocatalytic activity [28,29]. The above also facilitates the enhancement of the cooperative effect of TiO_2 and carbonaceous material boosting its adsorption property as well as photocatalytic activities from improved contact opportunity between pollutants and photocatalysts [29]. This also enhances the opportunity for photocatalyst's separation from the effluent and its reuse [29]. Biochar is a carbonized or charred product derived from biomass waste through thermal decomposition process [30]. It has high stability and can adsorb a large number of pollutants [31]. The high stability and semi-conductor properties of biochar further ensure that it offers good support to TiO_2 [32,33]. The synergistic interaction might enhance the photocatalytic efficiency of the TiO_2 if the compositing of the biochar composite is successful. Biochar also reacts as an electron acceptor that enhances the transfer of electrons from the TiO_2 and leads to the enhanced separation of electron-hole pairs.

Biochar-photocatalyst composite materials have aroused increasing attention in various environmental fields. Some composite materials that have been developed are TiO_2-coconut shell [34], TiO_2-Salvinia Molesta [35], TiO_2-reed straw [36], TiO_2-ramie char [37], TiO_2- corn cob [38], and TiO_2-bamboo [39], etc. At the same time, TiO_2_biochar composites have also demonstrated impressive potential to treat wastewater by degradation of organic pollutants through photocatalysis. For example, a study showed that the TiO_2-biochar composite achieved a 20 % higher photodegradation efficiency in the removal of methyl orange at a rate constant of 0.0226 min^{-1} than pure TiO_2 [40]. In similar conditions, TiO_2 functionalized biochar removed 99.5 % of methyl orange in 30 min [41]. Giant reed is a highly invasive grass species generated per year and is included among the 100 worst invasive species globally and has a potential high carbon yield, which is useful for biochar production. Due to its large surface area of 428.9 m^2/g and pore volume of 0.085 cm^3/g, giant reed biochar is potentially suitable for TiO_2 modification [42]. Besides the catalyst properties, other factors like phosphor, temperature, light intensity, reaction time, catalyst concentration, and pollutant concentration affect the photocatalytic efficiency [43]. The impact of factors such as pH, reaction time, catalyst dosage, and pollutant concentration on photocatalytic efficiency has not been extensively investigated concerning this specific composite [43]. In recent years, several optimization techniques have been applied in the engineering process for enhanced outcome accuracy. Of these, Response Surface Methodology (RSM) has turned out to be very useful in modeling and optimizing complicated experimental systems. Its primary benefit is the functional capacity to execute multiple experiments at once to save time and money when evaluating the impact of several variable factors [44]. RSM is different from the traditional approach that estimates the performance of the variables separately rather than considering their joint impact. RSM employs full quadratic models to predict the multiple parameters accurately according to various combinations of parameters making it more appropriate for accurate optimization, especially in the photocatalytic degradation research [45]. The qualitative data that was obtained via RSM in terms of response surface analysis and contour plots help in assessing the interactive behavior of the variables and decide on the best levels. Among the available RSM designs, Box-Behnken Design (BBD) and Central Composite Design (CCD) are the most commonly employed designs. CCD performs optimally when testing linear by-group interaction and quadratic effects, and it is versatile for expansion to higher factor spaces [46]. CCD is a useful technique for planning experiments and studying the main and interaction effects of factors with high accuracy, and for this reason, it was chosen for this study. Therefore, this research seeks to fill this gap by synthesizing a TiO_2-BC composite from giant reed biochar and enhancing the photocatalytic degradation of BB41 azo dye in wastewater under UV light using RSM model.

2. Materials and methods

2.1. Textile wastewater sampling and characterization

The wastewater samples were collected from the KK textile industry in Addis Ababa, Ethiopia. The collection process involved using plastic containers that were thoroughly cleaned with detergent, rinsed with tap water, soaked in 1 % HNO_3, and finally rinsed with distilled water to avoid contamination. The grab sampling method was used to collect wastewater samples and transport them to the laboratory to store at 4 °C to prevent any alterations before the analysis [47]. The wastewater characteristics were studied using certain water quality parameters such as temperature, pH, electrical conductivity (EC), turbidity, total dissolved solids (TDS), biochemical oxygen demand (BOD_5), chemical oxygen demand (COD), and others as detailed in Table 1.

2.2. Preparation of biochar and TiO_2-biochar composite

The Giant reed (Arundo donax L.) was initially crushed and air-dried which was further dried in an oven at 105 °C for 24 h. The dried biomass was milled using a hammer mill and screened through an 80–120 mesh sieve [42]. Then, the biochar was prepared via slow pyrolysis at a

Table 1
Selected textile wastewater physicochemical parameters and the analysis methods.

No.	Parameter	Methods and used instrument
1	Temperature	Hanna Multiparameter pH/EC/TDS/and Temperature (model HI98194).
2	pH	Multiparameter pH/EC/TDS/and Temperature (model Hanna- HI98194).
3	Color	Spectrophotometer (model Hatch DR3900)
4	EC	Multiparameter pH/EC/TDS/and Temperature (model Hanna- HI98194).
5	Turbidity	Turbidimeter (Model-TL2360) (0–10,000 NTU)
6	TDS	Multiparameter pH/EC/TDS/and Temperature (model Hanna- HI98194).
7	BOD_5	5210-BOD_5 Respirometric manometer
8	COD	Spectrophotometer (model Hatch DR3900)
9	BB41 Dye conc.	Shimadzu UV-3600PLUS spectrophotometer
10	NO_3^-	Spectrophotometer (model Hatch DR3900)
11	SO_4^{2-}	Spectrophotometer (model Hatch DR3900)
12	NH_4^+	Spectrophotometer (model Hatch DR3900)
13	PO_4^{3-}	Spectrophotometer (model Hatch DR3900)

heating rate of 10 °C/min in a nitrogen atmosphere (5 L/min) at 600 °C for 2 h in a muffle furnace [42]. TiO_2-biochar composites were synthesized via the sol–gel method using Titanium (IV) tetrachloride ($TiCl_4$, 99.5 %). Initially, 10 mL of $TiCl_4$ was added to 150 mL of distilled water in a 1000 mL beaker put in an ice bath, and stirred continuously for 10 min. Subsequently, 100 mL of ethanol (96 %) was added to the solution and stirred for another 20 min [48]. The experiment was carried out under a fume hood to ensure safety. Biochar was added to the solution at TiO_2-to-biochar weight ratios of 10:1, 10:2, and 10:3, then the mixture was stirred thoroughly to achieve uniform dispersion. Then the solution was titrated using 4 M NH_4OH solution until the pH reached 7.5 [49]. The mixture was allowed to settle overnight, and the supernatant was carefully decanted. The resulting gel was dried in a drying oven at 110 °C overnight. The dried material was ground with a mortar and pestle, then calcined at 600 °C for 2 h in a muffle furnace with a 10 °C/min heating rate under a 10 L/min nitrogen flow [48]. After cooling to room temperature, the composites were labeled as TBC-1, TBC-2, and TBC-3 based on their respective TiO_2-to-biochar ratios [48]. For comparison, bare TiO_2 was synthesized following the same procedure, excluding the addition of biochar.

2.3. Characterization of TiO_2-biochar composite

The BET-specific surface area of TiO_2 and TiO_2-biochar composites was assessed utilizing a Horiba SA-9600 surface area analyzer. The analysis of surface functional groups was conducted with an iS50 FTIR infrared spectrometer. The crystal phase of the composite was analyzed using a SHIMADZU XRD-6000 X-ray diffractometer. The crystallite size was subsequently determined using the Scherrer equation (Equation (1). Chemical structures and molecular interactions were examined using a WITec Raman spectrometer, which operated at 100X magnification, with a 532 nm laser and an output power of 5 mW. Surface morphology and surface elemental composition were evaluated through Scanning Electron Microscopy (SEM) (JSM-IT300 Joel, Tokyo, Japan) in conjunction with an EDX (Oxford X-MAXN) detector. The energy bandgaps were determined using a Shimadzu UV-3600PLUS spectrophotometer. The concept of the reflectance and bandgap are shown in Eqs. (2) and (3). Tauc's plot was employed to ascertain the bandgap of the composites, while the Kubelka-Munk equation was utilized to estimate the energy bandgap of TiO_2-biochar composites [50]. The point of zero charge (pHpzc) was determined via the salt addition method, where approximately 0.2 g of the sample was introduced into a 20 mL solution of 0.01 M NaCl within the 3–11 pH range [51].

$$D = \frac{K\lambda}{\beta\cos(\theta)} \quad (1)$$

$$F(R_\infty) = \frac{(1 - R\infty)^2}{2R_\infty} \quad (2)$$

$$(\alpha hv)^2 = B(hv - E_g) \quad (3)$$

Here, D is the average crystallite size (nm), K is the shape factor (usually 0.9), λ is the X-ray wavelength (1.5406 Å for Cu Kα), β is the FWHM in radians, and θ is the Bragg angle in radians. R∞ represents the reflectance of an infinitely thick specimen, α denotes absorbance, h is Planck's constant, ν stands for the photon frequency, B is a constant, and Eg refers to the bandgap energy.

2.4. Photocatalytic performances

Photocatalytic experiments were performed to evaluate the photodegradation efficiency of pure TiO_2 and TiO_2-BC composites. A 19 W UV lamp with a 254 nm wavelength was placed 25 cm over the reactor. In separate beakers, 0.1 g of TBC-2 composite and TiO_2 catalyst were added to 100 mL of a 20 mg/L Basic Blue 41 (BB41) dye solution. The mixtures were stirred in the dark for 30 min to achieve adsorption equilibrium. Afterward, the UV lamp was switched on, and the experiment was performed for 2 h. About 5 mL aliquots were taken out of the mixture at 30-, 60-, 90-, and 120-minute intervals. The mixture was then centrifuged at 8000 rpm, and the dye concentration was measured using UV–visible spectroscopy at 617 nm in the supernatant. In addition, a QbD1200 TOC Analyzer was used to analyze total organic carbon. Eqs. (4) and (5) were used to compute the degradation rates and mineralization efficiency.

$$\text{Removal}\,\% = \frac{C_0 - Ce}{C_0} * 100 \quad (4)$$

$$\text{TOC}(\%)\text{Removal} = \frac{(\text{in} - \text{TOC} - \text{f} - \text{TOC})}{\text{f} - \text{TOC}} * 100 \quad (5)$$

where Co represents the initial dye concentration (mg/L), Ce is the equilibrium concentration (mg/L), and TOC denotes total organic carbon, measured both before treatment (in-TOC) and after treatment (f-TOC), in mg/L.

2.5. Design of experiments

The photocatalytic efficiency was investigated based on the experimental design with the four operating factors Table 2. This was carried out by using the Central Composite Design (CCD) in Design-Expert software (Stat-Ease, Design-Expert 13). The CCD is a factorial combination with a minimum of four factors that were studied under the randomized response surface methodology. The impact of photocatalysis was used using four independent factors such as catalyst load (0.5–2.5 g), reaction time (30–150 min), solution pH (3–11), and initial dye concentration (10–50 mg/L). Each factor was evaluated at five distinct levels: (−α, −1, 0, +1, +α).

The number of experiments required is defined by Equation (6).

Table 2
Experimental design matrix for input variables and levels.

Factors	−alpha	Low (−1)	Mid (0)	High (+1)	+ alpha
pH	3	5	7	9	11
Catalyst load (mg/l)	0.5	1	1.5	3	2.5
Dye concentration (mg/l)	10	20	30	40	50
Time (min)	30	60	90	120	150

$$N = K^2 + 2k + Cp \quad (6)$$

where k is the number of factors and Cp is the number of central points.

The CCD for four input factors and five levels suggested a total of 30 experimental runs including 16 factorial points, 8 axial points, and 6 center points [52]. The factors and their levels as well as the response are presented in Table 3. The predicted response Y can be obtained from the quadratic model equation (7).

$$\gamma = \beta_0 + \sum_{i=1}^{k}\beta_i\chi_i + \sum_{i=1}^{k}\beta_{ii}\chi_i^2 + \sum_{i=1}^{k-1}\sum_{j>1}^{k}\beta_{ij}\chi_i\chi_j + \varepsilon \quad (7)$$

Here, γ represents the objective to optimize the response, bo is the constant term, bi is the linear coefficient, bii is the quadratic coefficient, bij is the interaction coefficient, k is the number of independent variables, and ε the error term. xi and xj represent the factors coded values.

The importance of the model and the evaluation of individual and interaction effects of the factors were examined using analysis of variance (ANOVA). The effectiveness of the model was determined by evaluating the R^2 coefficient, the adjusted R^2 coefficient, and the lack-of-fit test. The optimum conditions were identified by examining F-values and p-values, and three-dimensional response surface graphs were generated to illustrate the predicted results. Finally, TiO_2-BC composite was applied to remove the COD, turbidity, and color of textile wastewater using the optimum experimental point from the RSM study. The spectrophotometry method, specifically the HI 83099 COD and Multiparameter photometer from Hanna instruments was employed to determine the COD and color values of the effluent before and after treatment. The efficiency of COD removal and color removal were calculated using Eqs. (8) and (9).

$$\text{COD removal}\,\% = \frac{(COD_i - COD_f)}{COD_i} * 100 \quad (8)$$

$$\text{Color removal}\,\% = \frac{Color_i - Color_f}{color_i} * 100 \quad (9)$$

2.6. Determination of reactive species

Scavenging experiments were performed to determine the reactive species involved in the photodegradation of BB41 dye. These experiments compared the dye degradation rates in solutions without and with the presence of scavengers. Specifically, 0.05 mol of n-butanol (n-but) were used to scavenge hydroxyl radicals (•OH), 0.001 mol of ascorbic acid (AA) to target superoxide radicals ($\bullet O_2$), and 0.05 mol of oxalic acid (OA) to scavenge holes (h^+) [53].

2.7. Kinetics study and reusability of photocatalyst

The photocatalytic degradation kinetics of BB41 dye were evaluated under optimal experimental conditions using UV light. The degradation process was analyzed using zero-order, first-order, and second-order kinetic models (Eqs. (10)–(12)). Photodegradation experiments were conducted for 2 h, with 5 mL samples withdrawn at 20, 40, 60, 80, 100, and 120 min intervals [48]. A recycling test was performed under optimized conditions to assess the reusability of the photocatalyst. A measured quantity of the photocatalyst was added to a beaker containing the BB41 dye solution. After each photodegradation cycle, the supernatant solution was carefully extracted using a micropipette. Fresh BB41 dye solution was then introduced into the reaction beaker, and the process was repeated for a total of five cycles. All withdrawn samples were centrifuged at 8000 rpm to separate the catalyst, and the supernatant with residual BB41 dye was analyzed via UV–visible spectroscopy at 617 nm.

$$Ct = Co - kt \quad (10)$$

$$\ln\left(\frac{C_t}{C_o}\right) = -\text{kt} \quad (11)$$

$$\frac{1}{Ct} = \frac{1}{Co} + kt \quad (12)$$

where Co is the initial concentration, Ct represents the concentration at time (t), and (k) is the rate constant applicable to zero-order, first-order, and second-order reactions.

Table 3
Physiochemical characteristics of the textile wastewater.

No.	Parameter	Observed values
1	Temperature	45 °C
2	pH	5.61
3	Color	106 ± 2pt
4	EC	1605 μS/cm
5	Turbidity	48.55 ± 0.35 NTU
6	TDS	1105 mg/L
7	BOD_5	350 mg/L
8	COD	928 mg/L
9	BB41 Dye conc.	5.7 mg/L
10	NO_3^-	11.9 mg/L
11	SO_4^{-2}	47 mg/L
12	NH_4^+	15 mg/L
13	PO_4^{-3}	3.5 mg/L

3. Results and discussion

3.1. Physicochemical properties of textile wastewater

The physicochemical characteristics of wastewater from the KK textile industry were examined, with the findings summarized as mean values accompanied by standard deviations, as detailed in Table 3. The pH level of the effluent resulting from tanning processes was recorded at 5.61 ± 0.3, which falls below the permissible discharge range of pH 6–9 established by Ethiopian industrial standards [54]. This acidic pH indicates a potential risk of disrupting biochemical processes in the receiving aquatic environments. The average temperature of the effluent was noted to be 40 °C, which is consistent with the maximum allowable temperature for textile industrial effluents in Ethiopia [55]. Elevated temperatures in industrial discharges are generally regulated due to their capacity to enhance biochemical reaction rates in both terrestrial and aquatic ecosystems. Nevertheless, the recorded temperature adheres to the regulatory limits, suggesting that it is unlikely to significantly impact the biochemical and physicochemical dynamics within aquatic systems [56]. The Chemical Oxygen Demand (COD) and Biochemical Oxygen Demand (BOD_5) are essential indicators for evaluating the organic load in wastewater. The COD and BOD_5 values were found to be 928 ± 31 mg/L and 350 ± 12 mg/L, respectively, both surpassing the permissible thresholds of 250 mg/L and 60 mg/L [56]. The elevated COD levels point to the presence of toxic substances that may impede biological treatment processes [57]. This toxicity is likely attributable to the untreated heavy metals and organic compounds found in the textile wastewater [58]. The significant COD increase highlights the probable presence of toxicants, heavy metals, and persistent organic pollutants in the effluent [59]. Additionally, the BOD_5/COD ratio, often referred to as the biodegradability index, was determined to be 0.37, indicating a pressing need for biological or chemical treatment methods to reduce the organic matter concentration in the effluent [56]. The average values of Total Dissolved Solids (TDS) and Electrical Conductivity (EC) in the effluent were recorded at 1105 ± 11 mg/L and 1605 ± 45 μS/cm, respectively, both of which fall within the acceptable discharge limits of <1500 mg/L for TDS and <4000 μS/cm for EC [59]. Conversely, the effluent exhibited an average color measurement of 106 ± 2 Pt-Co units and a BB41 dye concentration of 5.7 ± 0.5 mg/L. The presence of elevated concentrations of azo dyes in the effluent presents considerable environmental and public health concerns. These dyes are known to be carcinogenic, resistant to aerobic degradation, and stable under

conditions of light, heat, and exposure to oxidizing agents, thereby complicating remediation efforts.

3.2. TiO_2-BC composite characteristics

3.2.1. FTIR spectrum analysis

The FTIR spectra of biochar (BC), TiO_2, and the TiO_2-biochar composite (TBC-2) are shown in Fig. 1. The spectrum of BC exhibits distinct bands at 1640 $cm^{-}1$ and 840–790 $cm^{-}1$, corresponding to aromatic C═C stretching and bending vibrations, respectively. These bands confirm the aromatic structure of BC. Upon carbonization, the disappearance of these characteristic peaks indicates the removal of surface functional groups, which might slightly reduce adsorption efficiency. However, this removal enhances BC's porosity, increasing its surface area [42]. The porous nature of BC significantly improves its adsorption capacity by providing more accessible adsorption sites for efficient pollutant capture. The FTIR spectrum of TiO_2 reveals an absorption band in the range of 600–400 cm^{-1}, attributed to the stretching vibrations of the Ti—O—Ti and Ti—O bonds within the TiO_2 molecule [60]. This confirms the successful synthesis of TiO_2. For the TBC-2 composite, a broad peak observed at 3395 cm^{-1} is assigned to the stretching vibrations of O—H bonds from phenolic, hydroxyl, and carboxyl groups, as well as adsorbed water on the catalyst's surface [40]. Notably, this peak is absent in the spectra of both BC and TiO_2, indicating a chemical interaction between the two components during composite formation. Additionally, a medium-intensity peak at 1640 cm^{-1} is observed in TBC-2, attributed to C═O and C═C vibrations from carboxylate and aromatic compounds present in biochar [61]. The absorption band in the 600–400 cm^{-1} range is also evident in the spectrum of TBC-2, corresponding to the stretching vibrations of Ti—O—Ti and Ti—O bonds [60]. This band is present in both TiO_2 and TBC-2 but absent in BC, further confirming the integration of TiO_2 into the composite. Notably, the absorption band of TiO_2, which appears at 450 and 430 cm^{-1} in its pure form, is shifted to 430 and 414 cm^{-1} in TBC-2. This shift, along with the reduced peak width, indicates a modification of TiO_2 bonds through the doping process. The formation of O—Ti—C bonds likely shortens the bond length of the Ti—O—Ti structure, further substantiating the interaction between TiO_2 and biochar in the composite [3]. These spectral features collectively demonstrate the successful synthesis and modification of the TBC-2 composite, highlighting its potential for enhanced photocatalytic and adsorption properties.

3.2.2. Surface area analysis

The surface area analysis of biochar, TiO_2, and the TiO_2-biochar composite was performed using a surface area analyzer. The results showed that the BET surface areas were 38 m^2/g for TiO_2, 428.98 m^2/g for biochar, and 118.89 m^2/g for the TiO_2-biochar composite. The addition of 20 % biochar significantly increased the surface area of the TiO_2 composite, demonstrating that integrating biochar enhances the composite's properties. This improvement is attributed to biochar's unique porous structure, which not only increases the overall surface area but also offers strong support for TiO_2 nanoparticles. The addition of biochar significantly influences the size of TiO_2 crystallites, serving as a nucleation site that facilitates the formation of smaller TiO_2 crystallites. Its porous structure also helps prevent particle agglomeration during synthesis [62]. Additionally, biochar enhances the dispersion of TiO_2 nanoparticles, promoting more uniform growth [63]. The resulting smaller TiO_2 particles exhibit a higher surface area-to-volume ratio, increasing the availability of active sites for chemical reactions and directly improving photocatalytic performance [29]. This enhancement makes the TiO_2-biochar composite highly effective for wastewater treatment applications [64]. The improved adsorption capability of the composite accelerates photocatalytic reactions. For example, studies have reported a surface area of 192 m^2/g for a TiO_2-biochar composite [65] and 34.2 m^2/g for an AC-TiO_2 composite [66]. Similarly, incorporating SiO_2 increased the specific surface area of an N-TiO_2 sample from 40.70 m^2/g to 115.4 m^2/g [67]. These findings emphasize the significant impact of adding biochar or other materials on the performance of TiO_2-based catalysts. The specific surface area of a composite depends on both the TiO_2 and biochar contributions. When designing photocatalysts, selecting materials that increase surface area is important to provide more active sites for efficient photodegradation reactions.

3.2.3. SEM-EDX analysis

SEM-EDX analysis was performed to characterize the

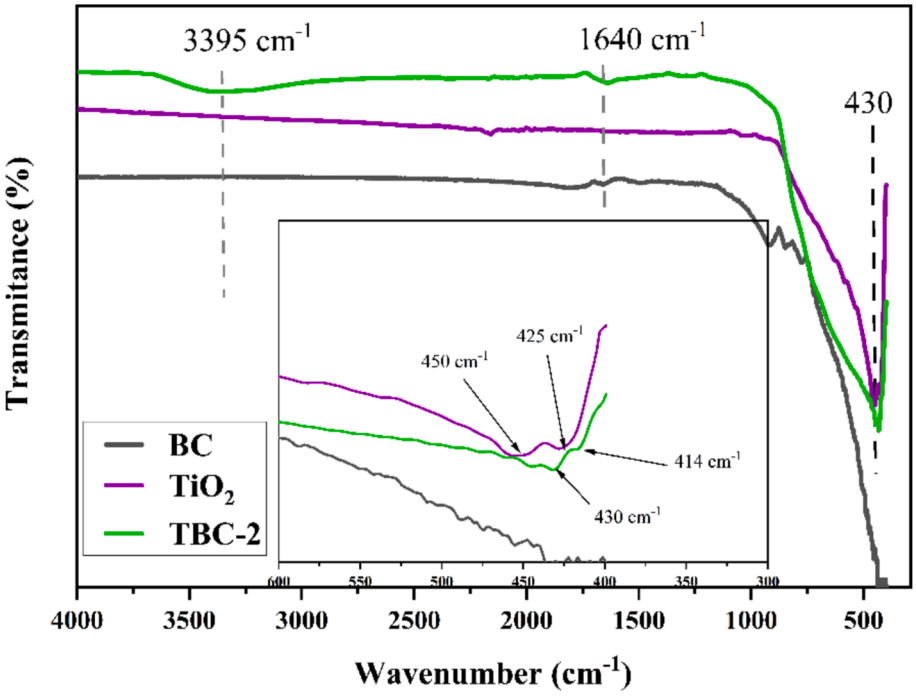

Fig. 1. FTIR spectra.

microstructures, morphologies, and elemental composition of the composite. Fig. 2(a–c) displays the SEM images of BC, TiO_2, and TiO_2-BC composite. The SEM image of BC reveals morphological fractures and a porous structure on its surface. This porous nature offers a high surface area-to-volume ratio, making BC an effective support for the TiO_2 photocatalyst and enhancing the degradation of dye pollutants from wastewater. The SEM image also reveals that pure TiO_2 particles appear smooth and blank, while TiO_2-BC composite particles exhibit a cracked and rough surface. The addition of biochar increased the agglomeration of TiO_2 particles on the biochar surface, with the TiO_2 particles being well dispersed within the biochar matrix. The rough and cracked surfaces present on the composite have been shown to increase the surface area and pore volume, which in turn promotes adsorption and improves the interaction between the catalyst and targeted pollutants [68]. This enhancement potentially accelerates the degradation process and simplifies the separation of photocatalysts from the effluent, enabling their repeated use [29]. Energy dispersive X-ray (EDX) analysis was performed to determine the available elements and their distribution in the composite. Fig. 2(d & e) shows the present elements in both TiO_2 and TiO_2-BC composite. The EDS analysis in Fig. 2d illustrates that the pure TiO_2 sample consisted of 57.8 wt% titanium and 43.2 wt% oxygen, whereas the TiO_2-BC composite exhibited titanium, oxygen, and carbon levels of 37.7 wt%, 34.3 wt%, and 28 wt%, respectively illustrated on Fig. 2e. The increased carbon content in the samples is likely due to the presence of biochar microparticles coating the TiO_2 nanoparticles [48]. The EDS analysis provides a surface microdomain examination, influenced by the sample surface depth, typically up to one micron below the surface [40].

3.2.4. *Uv–Vis DRS analysis*

The UV–Vis DRS spectra and bandgap energies for BC, TiO_2, and the TiO_2-BC composite are shown in Fig. 3. The BC shows stronger absorption in both the UV and visible light regions compared to TiO_2, indicating its good light-harvesting capability. In contrast, the TiO_2-BC composite demonstrates reduced UV light absorption relative to BC and TiO_2 but exhibits significantly enhanced visible light absorption compared to pure TiO_2, though slightly less than BC. This suggests that incorporating biochar into the TiO_2 matrix decreases UV absorption while broadening the material's absorption in the visible region. Notably, the TiO_2-BC composite exhibits a redshift, indicating an improved ability to absorb visible light compared to pure TiO_2. This enhanced light absorption can be attributed to the synergistic interaction between TiO_2 and biochar, as also reported in similar studies [69,70]. To further analyze the optical properties of the composite, the bandgaps (Eg) of BC, TiO_2, and TiO_2-BC were determined using Tauc plots (Eqs. (2) & (3)). The calculated bandgaps were 3.48 eV for BC, 3.03 eV for TiO_2, and 2.82 eV for TiO_2-BC, as shown in Fig. 3b. BC exhibits the widest bandgap, while TiO_2 shows a slightly lower value. However, the TiO_2-BC composite has the lowest bandgap among the three materials. This red shift in the bandgap is attributed to the interaction between TiO_2 and biochar, which modifies the electronic structure of TiO_2. The reduction in the bandgap of TiO_2-BC is attributed to the interaction between TiO_2 and biochar, which introduces new energy levels within the TiO_2 bandgap, effectively narrowing it [31]. Additionally, biochar acts as a Carbon dopant, introducing impurities into the TiO_2 lattice and creating further energy levels that enhance this effect [69,71]. Similar studies have also reported significant reductions in the bandgap of TiO_2 upon the addition of biochar, such as lowering anatase TiO_2 from 3.40 eV to 2.44 eV [50] and from 3.21 eV to 2.73 eV [70].

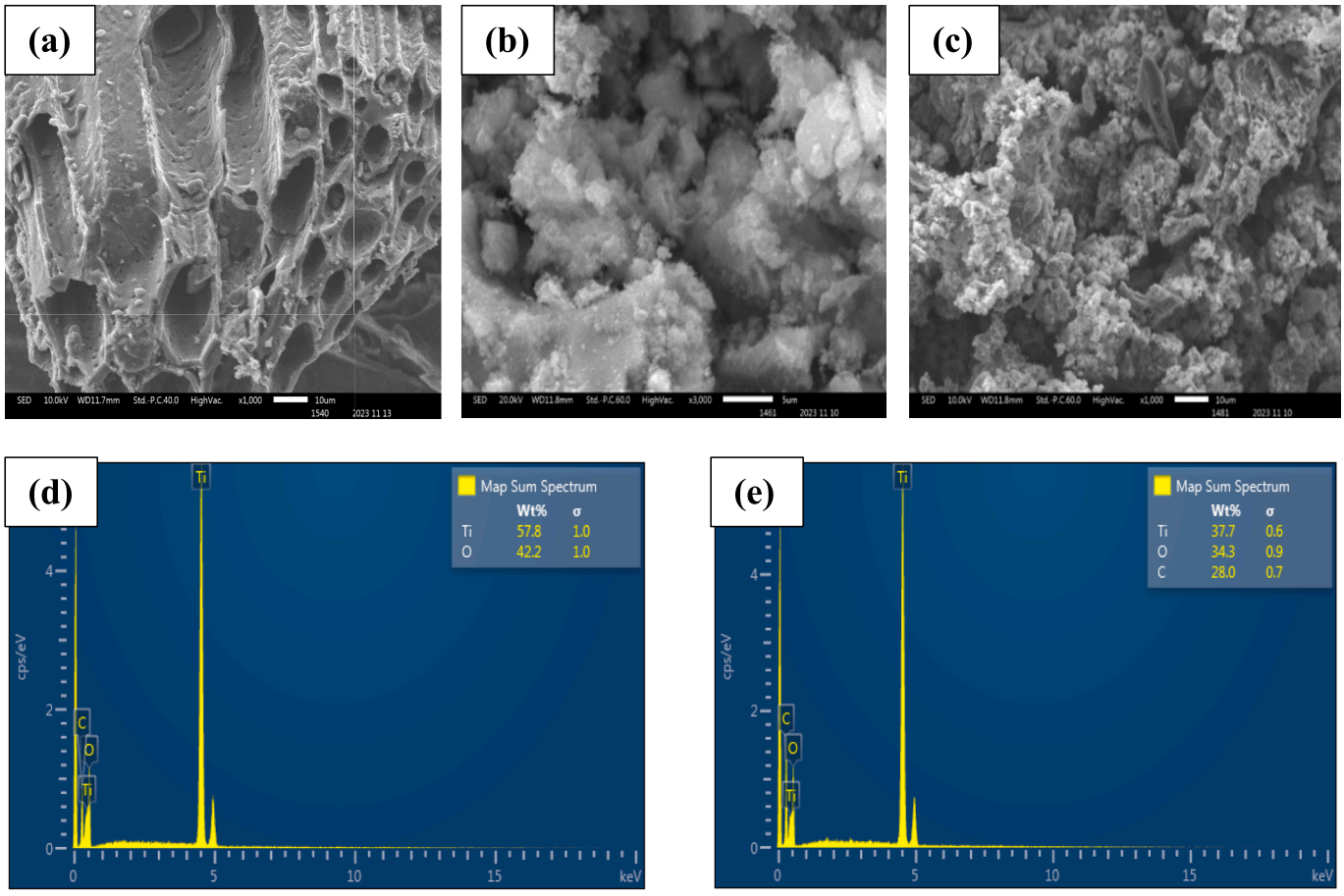

Fig. 2. (a–c) SEM image of BC, TiO_2, andTiO_2-BC and (d) EDS analysis of TiO_2, (e) EDS analysis of the TiO_2-BC composite.

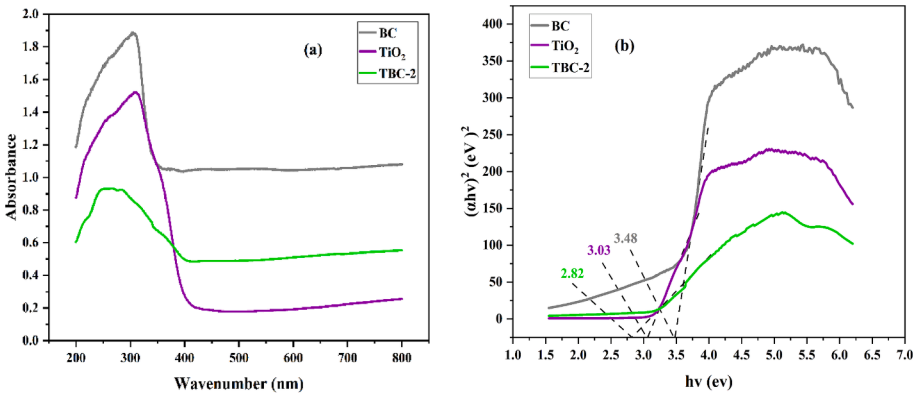

Fig. 3. (a) UV–vis diffuse reflectance spectra and (b) energy bandgap.

These results suggest that the TiO_2-BC composite has a broader absorption range than pure TiO_2, which improves its photocatalytic efficiency. The ability of TiO_2-BC to absorb light over a broader wavelength range underscores its potential for improved performance in photocatalytic applications.

3.2.5. Raman spectroscopy

Raman spectroscopy was used to analyze the structure of BC, TiO_2, and the TiO_2-biochar composite, as well as the carbon matrix. The Raman spectra for BC, TiO_2, and TiO_2-BC are shown in Fig. 4. The Raman spectrum of BC exhibits prominent peaks, including the D band at 1353 cm^{-1}, indicative of sp^2-carbon defects, the G band at 1590 cm^{-1}, corresponding to C—C bond deformation and aromatic ring vibrations, and the 2D band at 2826 cm^{-1}, which confirms the multilayered graphitic structure of BC [42]. The spectrum also reveals distinct peaks at 143 cm^{-1} (Eg), 196 cm^{-1} (Eg), 394 cm^{-1} (B1g), 514 cm^{-1} (A1g), and 634 cm^{-1} (Eg), which are characteristic of the anatase phase of TiO_2 [72]. This confirms the absence of peaks corresponding to rutile or brookite TiO_2 polymorphs in the TiO_2-biochar composite. The Raman spectra in Fig. 4 reveal two additional peaks, D and G, at 1350 cm^{-1} and 1595 cm^{-1}, respectively. These peaks are related to the presence of sp^3 C—C atoms and sp^2 C—C bonded Carbon molecules of Biochar [73]. The D peak is a defect-derived peak, which is caused by the disorder, while the G peak is a graphitic carbon. The addition of biochar showed noticeable peaks of biochar characteristics in the TiO_2-BC composite. The presence of BC reduced the intensity of the TiO_2 peaks. The reduction in peaks related to the TiO_2 catalyst indicates the successful integration of the TiO_2 nanoparticles with the biochar, resulting in the formation of the TiO_2-BC composite. This integration is essential for improving the catalytic properties of TiO_2, as the biochar serves as a stable support, facilitating the adhesion of the nanoparticles.

3.2.6. XRD analysis

The XRD patterns of BC, TiO_2, and TiO_2-BC composite are displayed in Fig. 5. The XRD of BC exhibits two broad peaks at 23.5 (C (0 0 2)) and 43.5° (C (1 0 0)), indicating the orientation of the aromatic carbon structures, as well as diffractions of graphitic and hexagonal carbons [74]. On the other hand, the XRD pattern of TiO_2 and TiO_2-BC composite shows diffraction peaks at 25.3°, 38.1°, 48.2°, 54.1°, 54.9°, 62.8°, 69.3°, and 75.4 which are indexed as (1 0 1), (0 0 4), (2 0 0), (1 0 5), (2 1 1), (2 0 4), (2 2 0), and (2 1 5) plane receptively and theses indicating that TiO_2 is anatase crystal type (PDF-2 00-064-0863). This illustrates that the addition of biochar does not notably alter the crystallographic structure of TiO_2. However, the introduction of biochar

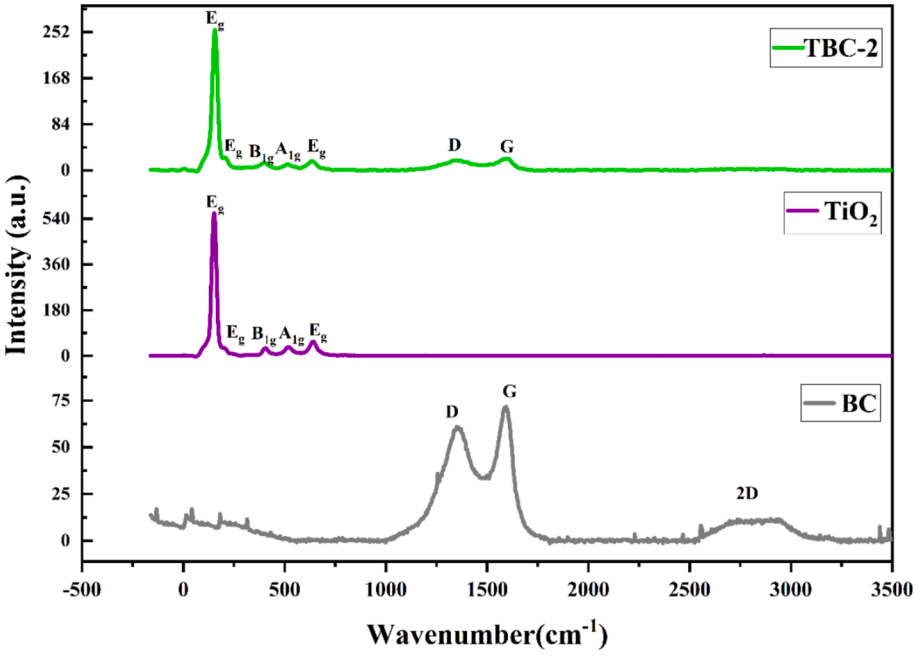

Fig. 4. Raman spectra.

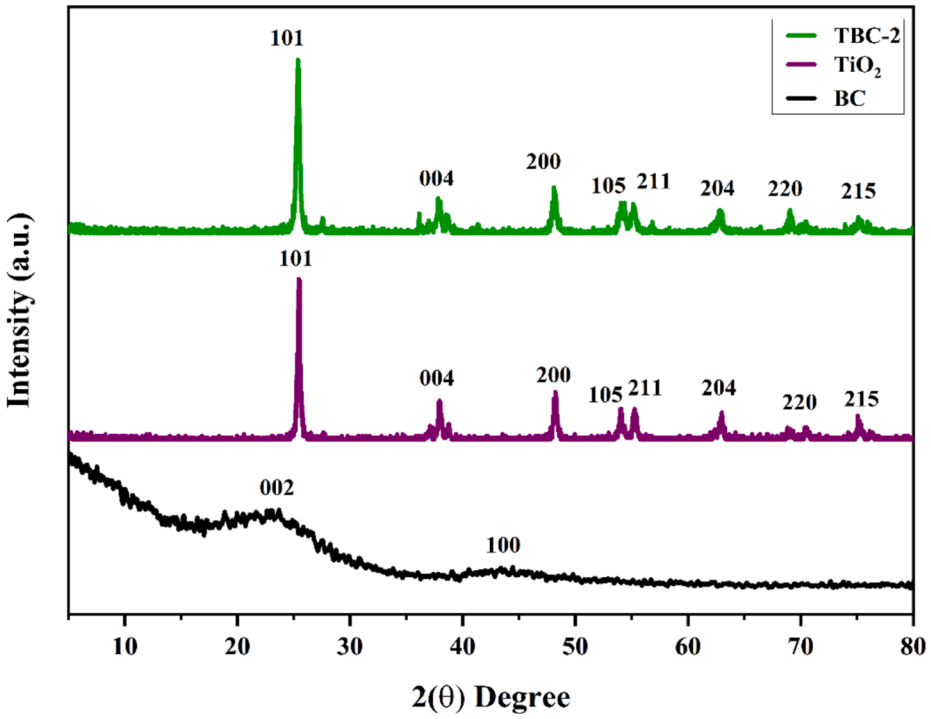

Fig. 5. X-ray diffraction (XRD) spectra.

has triggered a phase transition from anatase to rutile. However, the amount of rutile present is negligible. Moreover, it has been observed that the peaks of the TiO_2-BC composite are slightly broader in comparison to pure TiO_2, as shown in Fig. 5. This observation is consistent with a previous study [53,75]. The absence of the BC peak in the composites indicates that the anatase TiO_2 may have modified or obscured the graphitic carbon structure of the biochar [48]. This could be due to the shielding effect of the strong anatase TiO_2 peak on the weaker BC peak. Additionally, the photocatalytic and reactive properties of anatase TiO_2 may have influenced the chemical properties of biochar [53]. Conversely, incorporating biochar into TiO_2 catalysts decreases the crystallite size from 40.6 nm to 21.6 nm, improving the material's photocatalytic performance [76]. This reduction occurs due to multiple factors: biochar offers extra nucleation sites that facilitate the formation of smaller TiO_2 crystallites, and its porous structure prevents particle agglomeration during the synthesis process [62]. Biochar also affects the thermal properties by stabilizing smaller TiO_2 particles at high temperatures, while its functional groups can interact with TiO_2 precursors, altering the crystallization process [76]. Additionally, its large surface area and porous structure facilitate the uniform distribution of TiO_2 nanoparticles, leading to more consistent growth [63,77]. Smaller TiO_2 particles possess a higher surface area-to-volume ratio, providing more active sites for reactions and enhancing photocatalytic efficiency in wastewater treatment and air purification applications [64]. The reduced particle size also improves light absorption, charge separation, and quantum size effects, which decrease the band gap energy and enhance visible light utilization [78]. Furthermore, smaller crystallites enable better dispersion of TiO_2 within matrices, improving the performance of composites [79].

3.2.7. Point of zero charge

The determination of the point of zero charge (pHpzc) is crucial when analyzing the surface chemistry of a catalyst material and designing successful methods for water treatment. By analyzing the catalyst surface charge concerning the pH of water, we can effectively control the degradation process. Adsorbents below the pHpzc tend to attract contaminants with a negative charge, whereas those above it attract positively charged contaminants [80]. Fig. 6 illustrates the pHpzc of TiO_2 is approximately 5.56 and the pHpzc of biochar is recorded at 8.6. the result illustrates that TiO_2 has a positively charged surface below a pH of 5.56 and a negatively charged surface above it. The pHpzc of TiO_2 in this research is consistent with earlier studies [81], potentially influencing its practical applications. However, adding biochar shifted the pHpzc value from acidic to neutral, with TBC-2 showing a pHpzc of 6.86. This shift is influenced by biochar's pHpzc and its amount. The increase in pHpzc broadens the catalyst's applicability for both anionic and cationic pollutants, making it effective across a wider pH range. This versatility enhances the catalyst's effectiveness in removing contaminants from water and other environmental matrices.

3.3. Photodegradation experiment

The efficiency of BB41 dye photodegradation was evaluated using pure TiO_2 and TiO_2-biochar composite catalysts (TBC-1, TBC-2, TBC-3) under UV light irradiation. As shown in Fig. 7a, the degradation of BB41

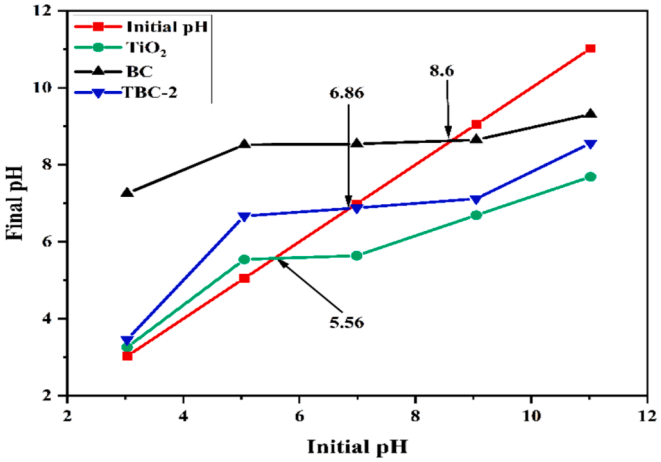

Fig. 6. Point of zero charges (pHpzc).

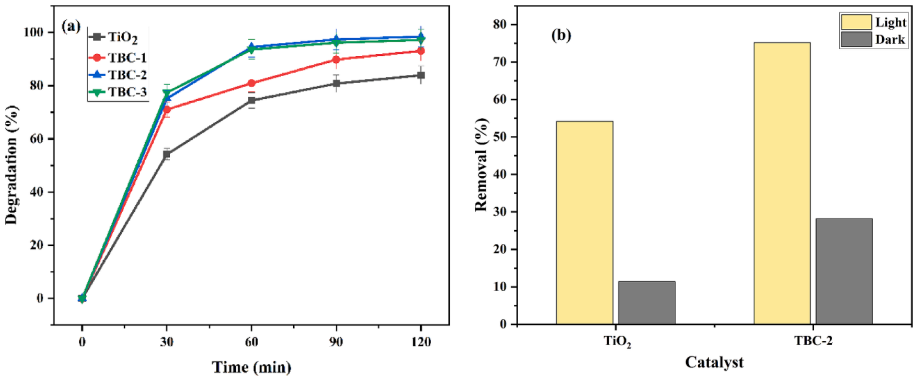

Fig. 7. (a) Comparative degradation efficiency of TiO_2, TBC-1, TBC-2, and TBC-3 composites, and (b) effects of dark and light reactions on the degradation rate. Experimental conditions: catalyst dose, 0.1 g; dye concentration, 20 mg/L; solution volume, 100 mL; time, 120 min and 30 min (dark and light reaction).

dye achieved only 83.9 %, 93.04 %, 98.42 %, and 97.2 % for pure TiO_2, TBC-1, TBC-2, and TBC-3, respectively. Notably, the TiO_2-biochar composite catalyst significantly enhanced the degradation efficiency. These results demonstrate the superior performance of the TiO_2-biochar composites compared to pure TiO_2. The incorporation of biochar improves the absorption of pollutants onto the catalyst surface and facilitates the transformation of photoelectrons, reducing the recombination of electron-hole pairs through the interaction between TiO_2 and biochar [29,40]. This interaction positively influences the photocatalytic oxidation process. Furthermore, the addition of biochar reduces the energy bandgap of the pure TiO_2 catalyst, promoting the generation of active species and enhancing photo-oxidation reactions [50]. However, The photocatalytic efficiency of biochar-doped TiO_2 catalysts decreases when the amount of biochar is above 20 wt%. Excessive biochar can saturate the surface area, limiting the number of active sites for pollutant adsorption [76]. Additionally, high biochar content can obstruct light penetration, reducing photocatalytic activity [82]. An imbalance in the TiO_2 to biochar ratio may disrupt electron transfer, further diminishing the photocatalytic efficiency [83]. Therefore, optimizing the biochar loading is crucial for improving the photocatalytic performance. in general, the TiO_2-biochar composite, especially TBC-2, demonstrates exceptional photocatalytic potential for the degradation of BB41 azo dye, with significantly higher BB41 98.42 % degradation rates compared to pure anatase TiO_2. Additionally, both dark and light reactions were conducted to investigate the reaction mechanism and determine whether the process involves adsorption or photocatalytic degradation. As shown in Fig. 7b, the removal percentages for the dark reaction were 11.4 % and 28.1 % for TiO_2 and TBC-2, respectively. For the light reaction, the removal percentages were 54.19 % and 75.17 % for the same catalysts under the same reaction time. These results indicate that the removal process is primarily governed by photocatalytic degradation rather than adsorption. However, the incorporation of biochar enhances the adsorption capacity of the TiO_2 catalyst, which contributes to the increased degradation and removal efficiency observed with the TBC-2 catalyst. This synergy between biochar and TiO_2 improves pollutant adsorption, facilitates electron transfer, and ultimately leads to superior photocatalytic performance.

Table 4
Central Composite Design Matrix for BB41 dye photocatalytic degradation.

Std	Run	Factor 1	Factor 2	Factor 3	Factor 4	Response 1
		A: pH	B: Catalyst Dose	C: initial dye concentration	D: time	Color removal %
		pH	g/L	mg/L	min	%
1	18	5	1	20	60	86.33
2	15	9	1	20	60	92.69
3	30	5	2	20	60	92.64
4	3	9	2	20	60	93.00
5	1	5	1	40	60	72.63
6	25	9	1	40	60	89.32
7	2	5	2	40	60	83.72
8	16	9	2	40	60	94.15
9	17	5	1	20	120	95.46
10	26	9	1	20	120	98.80
11	27	5	2	20	120	98.99
12	13	9	2	20	120	96.53
13	8	5	1	40	120	82.96
14	28	9	1	40	120	96.81
15	9	5	2	40	120	91.34
16	21	9	2	40	120	98.88
17	5	3	1.5	30	90	78.48
18	19	11	1.5	30	90	92.40
19	11	7	0.5	30	90	89.38
20	29	7	2.5	30	90	98.21
21	6	7	1.5	10	90	99.88
22	20	7	1.5	50	90	88.91
23	24	7	1.5	30	30	85.43
24	12	7	1.5	30	150	99.39
25	7	7	1.5	30	90	98.65
26	22	7	1.5	30	90	98.48
27	23	7	1.5	30	90	98.56
28	10	7	1.5	30	90	98.58
29	4	7	1.5	30	90	98.42
30	14	7	1.5	30	90	98.45

3.4. Model fitting and analysis of variance (ANOVA)

3.4.1. Model fitting analysis

The optimization of pH, catalyst dosage, dye concentration, and reaction time was carried out using Response Surface Methodology (RSM) with Central Composite Design (CCD) to enhance the degradation efficiency of BB41 dye, as detailed in Table 4. An analysis of variance (ANOVA) was performed to evaluate the statistical significance of the model. Table 5 identifies the quadratic regression model as the most appropriate for analyzing the photodegradation of BB41 dye, supported by the P-values, R^2, and F-value. The quadratic model yielded an F-value of 11,587.30 and a very small p-value (<0.01), demonstrating its high significance. The model's performance was further assessed using the coefficient of determination (R2) and adjusted R2, which showed excellent alignment, with R2 at 0.9999 and adjusted R2 at 0.9998. This indicates that the model can explain 99.99 % of the experimental data. The predicted R2 of 0.9996 closely matched the adjusted R2, signifying strong agreement between predicted and experimental outcomes. Additionally, the small coefficient of variation (C.V.%) of 0.09 % underscores the precision, reliability, and reproducibility of the experimental data. The Adequate Precision value of 415.7, far exceeding the acceptable threshold of 4, confirms the model's robustness in predicting BB41 dye degradation [84]. The ANOVA table for the quadratic model

Table 5
Analysis of variance (ANOVA) results for quadratic model.

Source	Sum of Squares	df	Mean Square	F-value	p-value	Significance
Model	1397.74	14	99.84	11587.30	<0.0001	**
A-PH	293.62	1	293.62	34077.33	<0.0001	**
B-Cat Dose	112.26	1	112.26	13029.50	<0.0001	**
C-[C]	184.68	1	184.68	21433.42	<0.0001	**
D-time	288.58	1	288.58	33493.07	<0.0001	**
AB	37.13	1	37.13	4308.97	<0.0001	**
AC	104.58	1	104.58	12137.27	<0.0001	**
AD	8.36	1	8.36	970.25	<0.0001	**
BC	21.35	1	21.35	2478.14	<0.0001	**
BD	7.33	1	7.33	850.35	<0.0001	**
CD	1.60	1	1.60	185.34	<0.0001	**
A^2	293.27	1	293.27	34036.51	<0.0001	**
B^2	38.26	1	38.26	4440.87	<0.0001	**
C^2	29.16	1	29.16	3384.52	<0.0001	**
D^2	64.03	1	64.03	7431.12	<0.0001	**
Residual	0.1292	15	0.0086			
Lack of Fit	0.0907	10	0.0091	1.18	0.4547	##
Pure Error	0.0385	5	0.0077			
Cor Total	1397.87	29				

$R^2 = 0.9999$, Adj. $R^2 = 0.9998$, Pre. $R^2 = 0.9996$, C.V.% = 0.099, Adeq Precision = 415.7, Significant = **, and Not-significant = ##.

highlights the significance of various model terms and their impact on degradation efficiency [85]. Table 5 further illustrates that the large F-value and small p-value (<0.05) validate the model's ability to explain variations in degradation efficiency. P-values for individual terms indicate statistical significance, with factors A (pH), B (catalyst dosage), C (dye concentration), and D (degradation time), along with interactions AB, AC, AD, BC, BD, and quadratic terms A2, B2, C2, and D2, were found to be substantial contributors. The small p-values associated with these variables confirm their significant impact on degradation efficiency. The Lack of Fit F-value of 1.18 indicates that the Lack of Fit is not statistically significant compared to pure error, with a 45.47 % probability of the observed Lack of Fit F-value being due to noise. A non-significant Lack of Fit suggests the model adequately fits the data, with any discrepancies between observed and predicted values likely attributable to random variation rather than model inadequacy [86]. This result supports the model's capacity to accurately represent the relationship between variables without requiring further complexity. With a p-value exceeding the chosen significance level (0.05), the Lack of Fit test confirms the model's adequacy, indicating that residuals are randomly distributed and predictions align closely with observed data [44,87]. Hence, a quadratic equation (Eq. (13)) was employed to estimate the photocatalytic efficiency for BB41 dye oxidation, incorporating the identified independent variables.

$$\text{Color removal}\,\% = 98.52 + 3.49{*}A + 2.16{*}B - 2.77{*}C + 3.46{*}D - 1.52{*}AB + 2.55{*}AC - 0.72{*}AD + 1.15{*}BC - 0.67{*}BD + 0.31{*}CD - 3.26{*}A^2 - 1.18{*}B^2 - 1.03{*}C^2 - 1.52{*}D^2 \quad (13)$$

where A is the pH of the solution B, is the catalyst dose, C is the initial concentration of the dye, and D is the reaction time.

The effect of a variable refers to the change in the outcome resulting from altering the level of that variable. The above formula (Eq. (13)) represents a second-order polynomial equation (coded based on factors) for the analyzed response, with the intercept coefficient of the model set at 98.52. The decolorization efficiency improves as the pH, catalyst dose, and reaction time increase, with positive coefficients of 3.49, 2.16, and 3.46, respectively. This happens because a higher amount of catalyst provides more active reaction sites, and increasing the pH enhances the interaction between the cationic BB41 dye and the catalyst surface. Higher pH levels also promote the production of hydroxyl free radicals, which further boost degradation. Similarly, giving the reaction more time ensures the dye and catalyst have enough time to interact fully, leading to better results. On the other hand, a higher dye concentration has a negative effect on efficiency, as shown by its negative coefficient of 2.77. This is likely because when there's too much dye, the catalyst's active sites get saturated and can't keep up with the excess, reducing overall effectiveness. The interaction effects (AC), (BC), and (CD) positively influence the process, with coefficients of 2.55, 1.15, and 0.31, respectively. In contrast, the interaction effects (AB), (AD), and (BD), along with the quadratic terms (A2), (B2), (C2), and (D2), exhibit negative coefficients of −1.52, −0.72, −0.67, −3.26, −1.18, −1.03, and −1.52, respectively. Synergistic relationships are indicated by positive interaction effects, where the combined influence of two variables surpasses the sum of their impacts. Conversely, negative interaction effects imply that specific variable combinations or elevated levels of individual factors may negatively impact the process. The p-values determine the significance of all factors, as shown in Table 5 the p-values for the linear factors and their interactions with the other factors are lower than 0.05, indicating significance towards the degradation of BB41 dye. Additionally, the sum of squares (SS) from the ANOVA data was used to calculate the total percentage contributions (TPC) of each factor, showing how much each factor explains the variance. Fig. 8 reveals that individual, interaction, and quadratic effects all impact degradation efficiency. pH is the most influential factor, followed by the quadratic effect of pH, degradation time, dye concentration, and catalyst dose. Among interactions, pH and dye concentration have the greatest impact, while other effects contribute less than 5 %. Optimizing these key variables can greatly enhance BB41 dye degradation efficiency.

$$\text{Contribution} = \left(\frac{\text{Sum of Squares}}{\text{Total Sum of Squares}}\right){*}100$$

3.5. Model validation

A validation assessment is essential to develop an accurate mathematical model [48]. The model's validity was verified by comparing the predicted and actual experimental responses [88]. Fig. 9a illustrates a graph of the actual values versus the predicted values, indicating that all data points were dispersed and followed a normal distribution around the linear regression line. This normality in distribution verifies that the residuals are properly distributed. Fig. 9b illustrates the residual normal probability plot, confirming that the residuals adhere to a normal distribution. Meanwhile, Fig. 9c depicts the scatter plot of residual values against predicted values, revealing a random pattern with no discernible trends or significant variance, indicating the absence of heteroscedasticity. Furthermore, Fig. 9d presents the Internally Studentized Residuals plot, which shows no outliers or abnormal data points. These

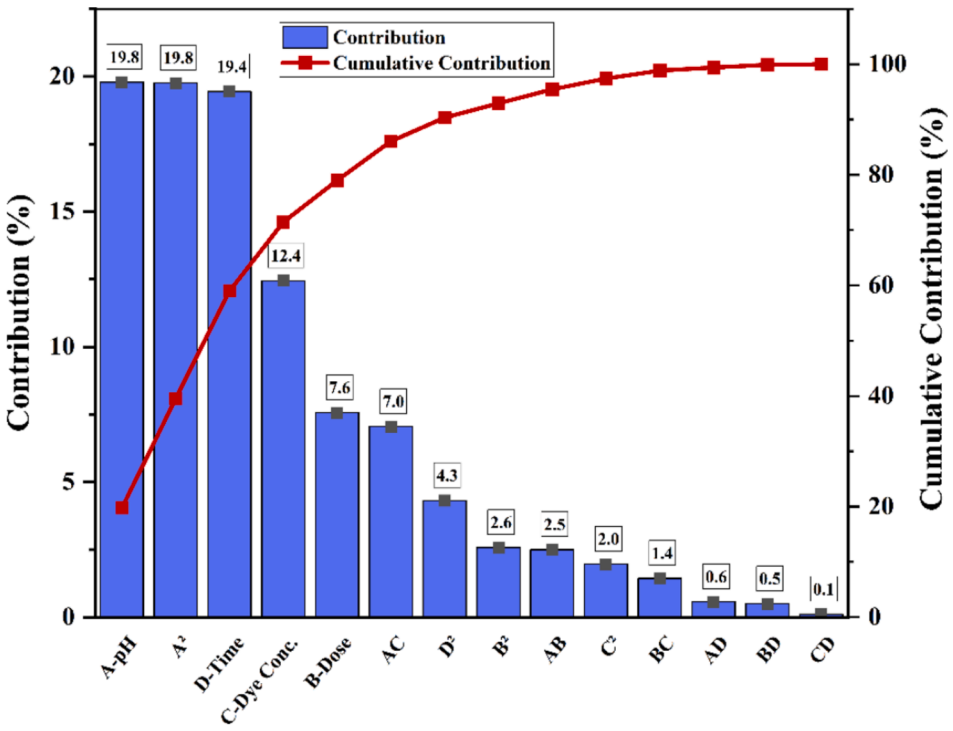

Fig. 8. Schematic representation of the Percentage Contribution.

results collectively validate the reliability and appropriateness of the CCD model in optimizing the photodegradation process of BB41 dye.

3.6. Effect of individual factors

The response surfaces are illustrated through a quadratic regression equation and detailed graphical representations. These 3D and contour plots are depicted in Fig. 10(a–d) provide a comprehensive understanding of the significant impacts of individual and interaction factors on the response, as well as the interactions between each factor. Specifically, the graphs show the individual factor pH (A), catalyst dose (B), initial concentration (C), and time (D) effects of and the interaction factors on degradation efficiency. The photodegradation efficiency of Basic Blue 41 (BB41) dye is significantly impacted by the pH of the solution. The study reveals that as the solution's pH increases from 3 to 8.15, the photodegradation efficiency of BB41 improves, rising from 78.4 % to 99.5 %. However, beyond a pH of 8.15, the degradation efficiency starts to decline, dropping from 99 % to 92.4 % at pH 11. This variation in photodegradation efficiency can be attributed to several factors. For instance, the surface charge of the photocatalyst, also known as the point of zero charge (pHzpc) for the composite, is 6.86. Below this pH, the surface of the composite is positively charged, leading to reduced adsorption and lower photodegradation efficiency. In contrast, at pH levels above the pHzpc, the negatively charged surface of the TiO_2-BC composite enhances the electrostatic attraction between the surface and the BB41 dye, improving dye adsorption and, consequently, degradation efficiency [89]. Additionally, in alkaline conditions (pH > 6.86), the concentration of hydroxide ions (OH^-) rises, promoting the generation of highly reactive hydroxyl radicals (•OH), which enhance the photodegradation process [90]. However, at very high pH levels (above 8.8), the excessive hydroxide ions can act as scavengers of these hydroxyl radicals, reducing their availability for degrading the dye molecules, leading to a decrease in photodegradation efficiency at higher pH values [91]. In general, the pH of the solution influences the surface properties of the photocatalyst, the distribution of charge on organic molecules, and the formation of reactive radical species, which all are crucial to the photocatalytic degradation process. Catalyst dosage is a crucial factor in photodegradation studies, as it directly impacts the catalyst's effectiveness. The results indicate that as the catalyst dose increases from 0.5 g/L to 1.95 g/L, the degradation efficiency of BB41 dye improves significantly, rising from 89.4 % to 99.7 %. This improvement is due to the increased number of active sites and electron-hole pairs, which generate more reactive hydroxyl radicals, enhancing mass transfer and photodegradation [88]. However, beyond the optimal dose of 1.95 g/L, the degradation efficiency begins to decline, dropping to 98.1 % at 2.5 g/L. This decrease in efficiency is attributed to catalyst agglomeration at higher dosages, which reduces the available surface area for dye molecules to interact with the catalyst. Additionally, excessive catalyst amounts can cause increased light scattering within the solution, reducing the penetration of UV or visible light needed to activate the photocatalyst. Consequently, fewer photons reach the catalyst particles, leading to a lower generation of electron-hole pairs and ultimately reducing the degradation rate [92]. A similar result reported that the degradation of RV5 Azo Dye on Fe-Doped Titania Catalysts (0–6 g/L) under visible light irradiation showed a consistent degradation rate after reaching 3 g/L [93]. Therefore, it is essential to add the optimal amount of catalyst to achieve efficient photodegradation. The initial dye concentration has a significant impact on the photodegradation efficiency of BB41 dye. As shown in Fig. 10C, the degradation efficiency remains constant at 100 % when the dye concentration increases from 10 mg/L to 25 mg/L but declines sharply to 80.8 % as the concentration further increases to 50 mg/L. The reduced efficiency at higher dye concentrations can be explained by several interconnected factors. Firstly, the photocatalyst has a limited number of active sites where the degradation reaction occurs. As the dye concentration rises, more BB41 molecules compete for these active sites, resulting in fewer molecules being adsorbed and degraded [92,94] Additionally, at higher concentrations, the solution becomes more intensely colored, leading to increased light absorption by the dye itself, a phenomenon known as the inner filter effect, which reduces the amount of light reaching the photocatalyst and thus lowers the generation of electron-hole pairs necessary for degradation [95]. Furthermore, increased dye concentration causes greater light scattering within the solution, reducing light penetration to deeper layers and limiting the

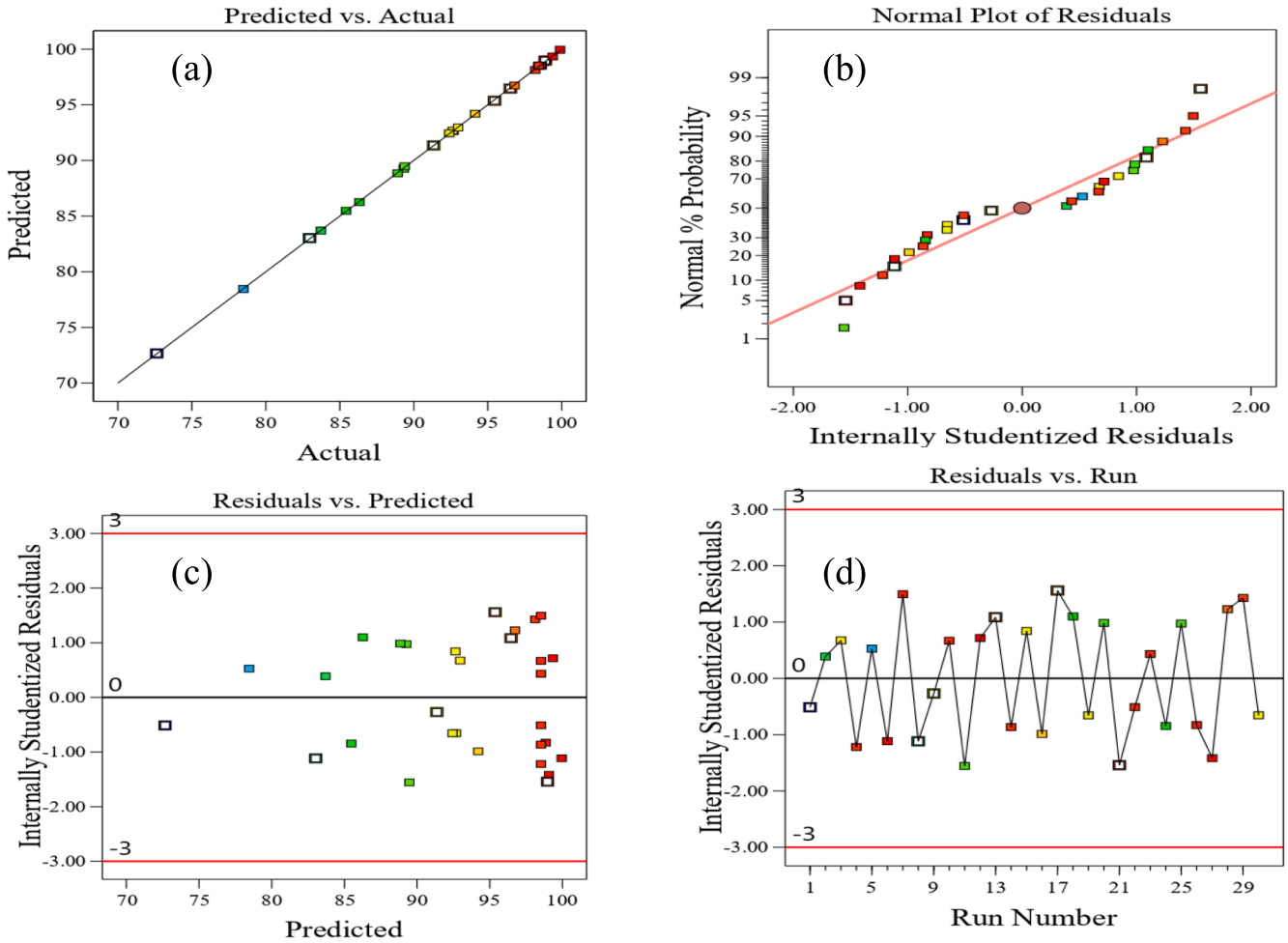

Fig. 9. (a) Plots of actual values versus predicted value, (b)Normal plot of residuals, (c)The internally Studentized Residuals versus predicted ones, and (d) The Internally Studentized Residuals versus run number.

activation of photocatalyst particles not directly exposed to the light source [96]. At even higher concentrations, dye molecules may saturate the photocatalyst surface, hindering the interaction between the catalyst, light, and the surrounding environment, which further decreases the overall photodegradation efficiency [94]. The results demonstrate in Fig. 10D that the photodegradation efficiency increased from 85.4 % to 100 % as the reaction time was extended from 30 to 115 min, remaining constant until 135 min. After 135 min, a slight decrease in efficiency to 99.3 % was observed. The degradation percentage generally rises with increased reaction time, peaking at 120 min. This improvement is attributed to prolonged UV irradiation, which allows the photocatalyst to absorb more photon energy, thereby enhancing the photodegradation process. Extended irradiation also boosts the generation of hydroxyl radicals, which are crucial for oxidizing organic pollutants and breaking them down into simpler molecules [97]. However, while longer reaction times typically improve photodegradation efficiency, a slight decline after a prolonged period may occur due to factors such as the depletion of reactive species, recombination of electron-hole pairs, catalyst saturation, formation of stable by-products, dye re-adsorption, and catalyst deactivation. These factors can contribute to a decrease in efficiency after extended reaction times [98].

3.7. The interaction effects on the photocatalytic degradation

3.7.1. pH and the catalyst dose

The interactive effects between variables are important to consider for true optimization, rather than relying solely on the One-Factor-At-a-Time (OFAT) method. Analyzing these interactions provides a more comprehensive understanding of the system's behaviour [99]. Contour plots visually depict how changes in one variable can influence the effect of another. Understanding and identifying these interactions are crucial for refining processes and ensuring reliable and maximized experimental outcomes. The interaction between pH and catalyst dosage on BB41 removal, As illustrated in Fig. 11, a strong correlation is demonstrated through a three-dimensional and contour plot. This study investigated pH levels between 3 and 11, with catalyst dosages varying from 0.5 to 2.5 g/L, while keeping the dye concentration constant at 30 mg/L and the irradiation time fixed at 90 min. The results reveal that the interaction significantly enhances BB41 degradation, achieving the highest efficiency (99 %) within the pH range of 7 to 9 and a catalyst dose between 1.4 and 2 g/L. In contrast, the lowest efficiency (~70 %) was observed at a pH of 3 and a catalyst dose of 0.5 g/L. The analysis shows that increasing both pH and catalyst dosage enhances degradation efficiency. Higher catalyst doses provide more active sites and electron-hole pairs, while elevated pH promotes the formation of reactive hydroxyl radicals [90]. The interaction is closely linked to the point of zero charges (pHzpc) of the TiO_2-biochar composite, which governs surface charge dynamics and electrostatic interactions [88]. Additionally, increasing the catalyst dosage enhances the available surface area, leading to better interaction between the dye and the catalyst. As the pH increases from 3 to 9, the required catalyst dose decreases from 2.5 to 1. g/L, optimizing the photocatalytic process by balancing pH and dosage, resulting in reduced catalyst consumption while maintaining high degradation efficiency.

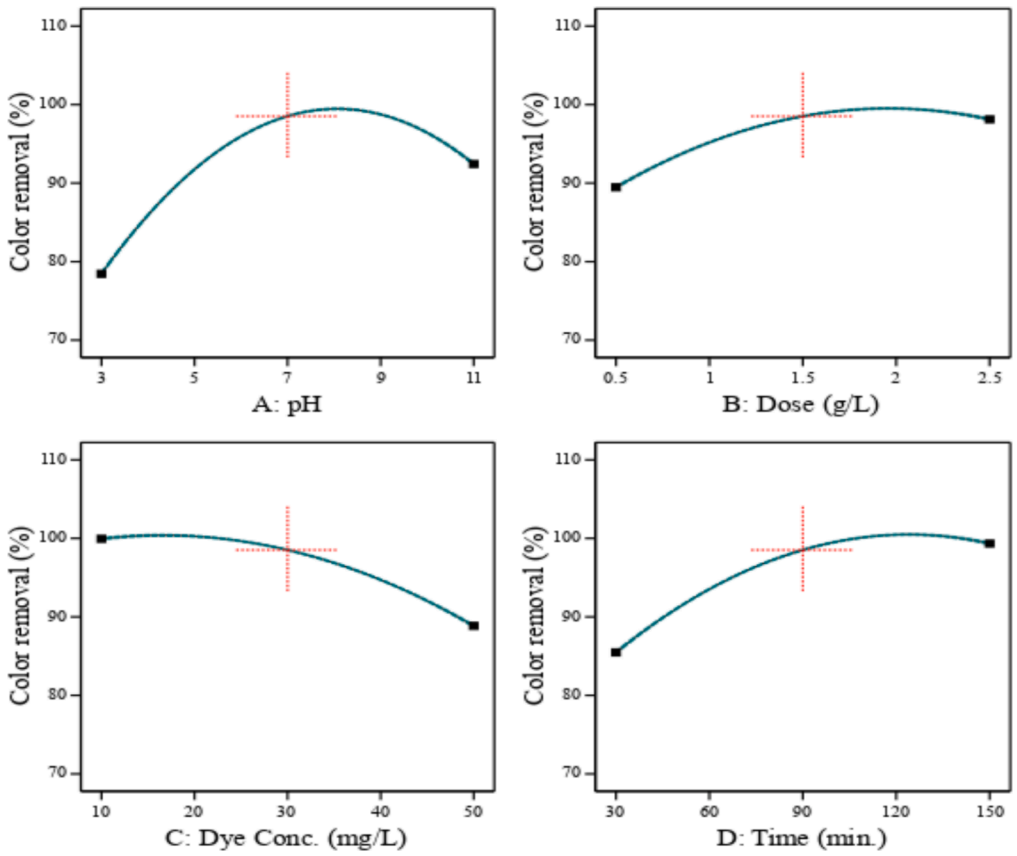

Fig. 10. Effect of individual factors: (A) pH, (B) catalyst dose, (C) initial dye concentration, and (D) irradiation time.

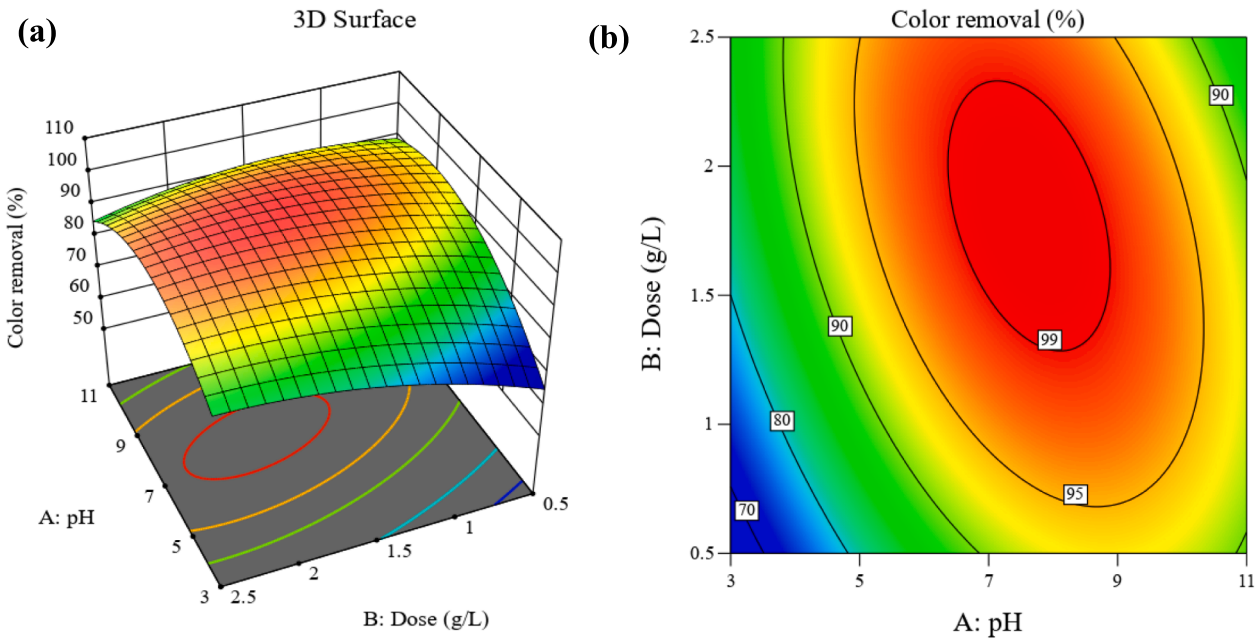

Fig. 11. Effect of pH and catalyst dose: (a) 3D surface plot and (b) contour plot.

3.7.2. pH and initial dye concentration

The interaction effect between pH and initial dye concentration on the removal efficiency of BB41 dye is presented in Fig. 12 through three-dimensional response surface and contour plots. The analysis covered a pH range of 3–11 and initial dye concentrations between 10 and 50 mg/L, with the catalyst dosage fixed at 1.5 g/L and an irradiation time of 90 min. The results demonstrate that the degradation efficiency is strongly influenced by the interaction between the pH of the solution and the initial dye concentration. The highest degradation efficiency (99 %) was achieved at a pH of 5–9 with a dye concentration of 10–32 mg/L. On the other hand, at a pH of 3 and a dye concentration of 50 mg/L, the lowest degradation (~63 %) was observed. As the dye concentration increased,

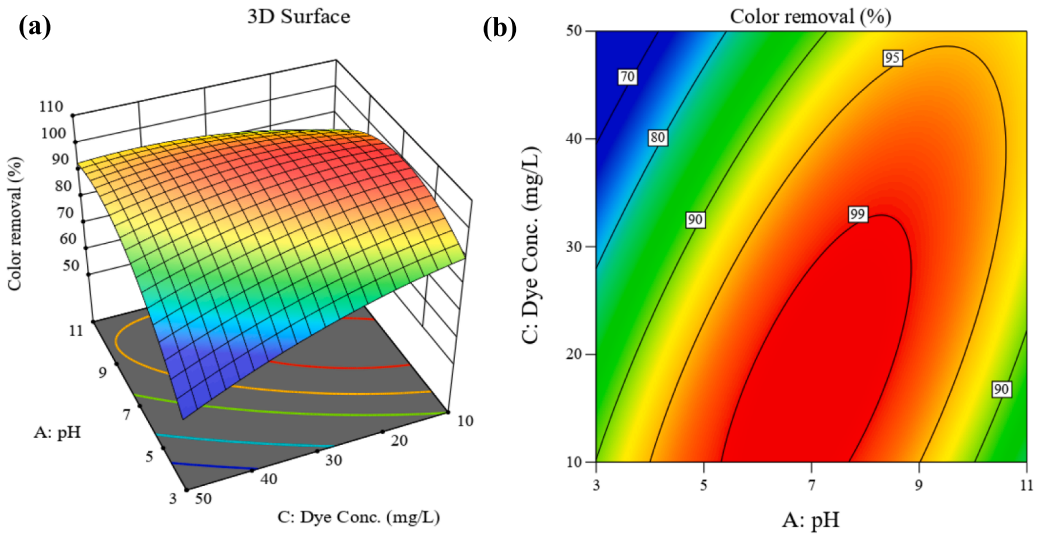

Fig. 12. Effect of pH and initial dye concentration: (a) 3D surface plot and (b) contour plot (b).

the degradation efficiency decreased, while increasing the pH led to improved efficiency. This is because, at pH levels above 6.86, TiO_2 acquires a negative surface charge, which enhances its ability to adsorb BB41, a cationic dye [88]. Additionally, hydroxyl radicals are more readily generated in neutral and basic conditions, further promoting dye degradation [90]. Optimizing both pH and initial dye concentration allows for better control of the photocatalytic process, ensuring efficient degradation across a broader range of dye concentrations and pH levels.

3.7.3. *pH and irradiation time*

The interaction between pH and irradiation time on BB41 dye removal, illustrated in Fig. 13, demonstrates a significant correlation through a three-dimensional plot. The study evaluated pH levels from 3 to 11 and irradiation times ranging from 30 to 150 min while keeping a constant catalyst dosage of 1.5 g/L and an initial dye concentration of 30 mg/L. The results reveal that BB41 degradation efficiency is strongly influenced by the interaction between pH and irradiation time. The highest degradation efficiency (99 %) was achieved at a pH of 8 with an irradiation time of 90 min. In contrast, at a pH of 3 with a degradation time of 30 min the lowest efficiency (~65 %) was observed. As the pH increased from 3 to 8, the required irradiation time decreased from 120 to 90 min. Moreover, extending the irradiation time helped maintain efficiency within neutral and acidic pH ranges. Longer irradiation times result in the generation of more reactive radicals, which enhance the degradation process [97]. Adjusting both pH and irradiation time offers better control over the photocatalytic process, ensuring optimal degradation efficiency across a broad range of pH values and reaction durations.

3.7.4. *Catalyst dosage and initial dye concentration*

Fig. 14 illustrates the interaction between catalyst dosage and initial dye concentration on BB41 removal, highlighting a significant correlation depicted through three-dimensional response surface and contour plots derived from RSM analysis. Catalyst doses of 0.5–2.5 g/L and dye concentrations of 10–50 mg/L were tested, with pH 7 and a 90-minute irradiation time. The highest degradation efficiency (99 %) was achieved at a catalyst dose of 1–2 g/L and dye concentrations between 10 and 30 mg/L. However, as the initial dye concentration increased from 30 mg/L to 50 mg/L, degradation efficiency declined. Optimal removal occurred at a catalyst dose of 1.9 g/L, resulting in 99 % degradation of 30 mg/L BB41 dye. Increasing the catalyst dose from 0.5 to 2.5 g/L enhanced the amount of dye degraded, as the higher photocatalyst

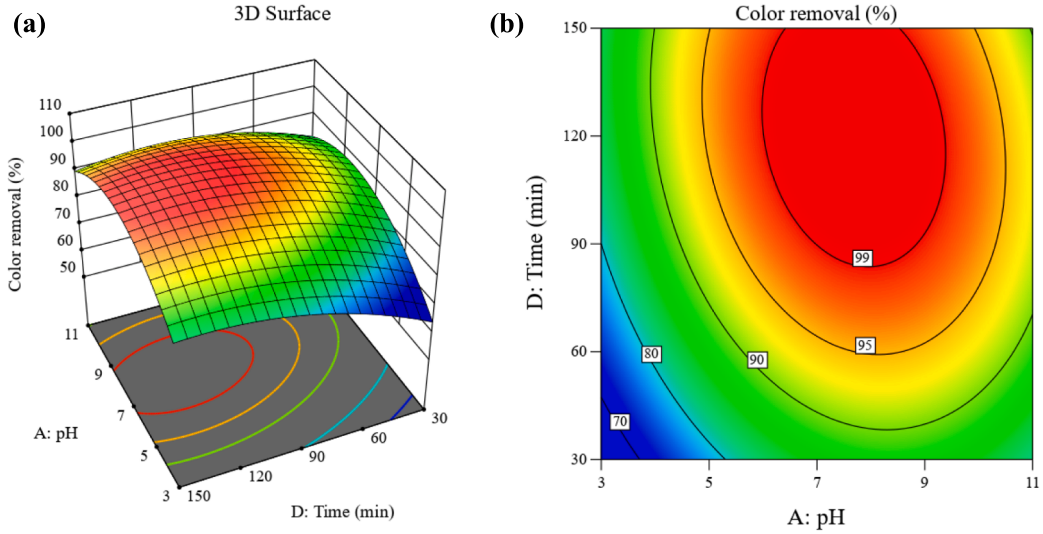

Fig. 13. Effect of pH and reaction time: (a) 3D surface plot and (b) contour plot.

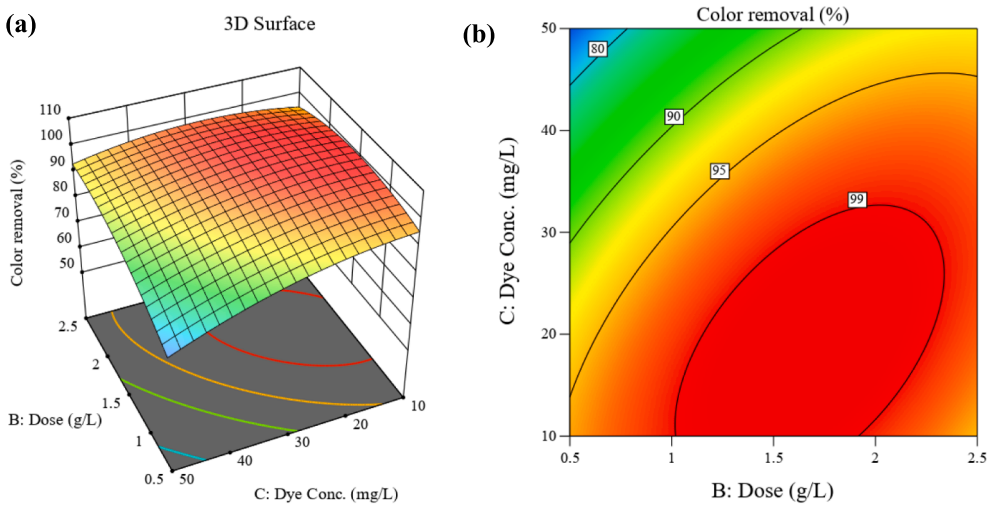

Fig. 14. Effect of catalyst dose and initial dye concentration: (a) 3D surface plot and (b) contour plot.

dosage provided more active sites and an expanded surface area, facilitating greater production of hydroxyl radicals. These radicals significantly boost the photocatalytic degradation of BB41 dye [88]. By adjusting both the catalyst dose and initial dye concentration, the photocatalytic process can be effectively carried out, enabling efficient performance over a wider range of dye concentrations the photocatalytic process can be achieved, allowing efficient operation across a broader range of dye concentrations while optimizing catalyst utilization and minimizing unnecessary consumption.Fig 15.

3.7.5. *Catalyst dosage and irradiation time*

Fig. 14 illustrates the interaction between catalyst dosage and reaction time on BB41 removal, highlighting a significant correlation depicted through three-dimensional response surface and contour plots derived from RSM analysis. Catalyst doses (0.5–2.5 g/L) and irradiation times (30–150 min) were tested at pH 7 with a 30 mg/L dye concentration. Maximum degradation efficiency (99 %) occurred at 1.2–2.4 g/L catalyst and 90–120 min irradiation. Increasing the catalyst dose enhanced the number of active sites, leading to greater production of hydroxyl radicals, while extended irradiation time further increased radical generation. These factors combined to significantly boost BB41 degradation efficiency [88,97]. Notably, the degradation time decreased from 120 to 90 min when the catalyst dose increased from 1.2 to 2 g/L. Conversely, increasing the irradiation time from 90 to 120 min reduced the required catalyst dose from 2 g/L to 1.2 g/L for the same level of efficiency. This inverse relationship shows that optimizing either catalyst dose or irradiation time can enhance degradation performance while minimizing resource use. Carefully adjusting both parameters allows for better control over the photocatalytic process, ensuring efficient dye removal without unnecessary catalyst consumption.

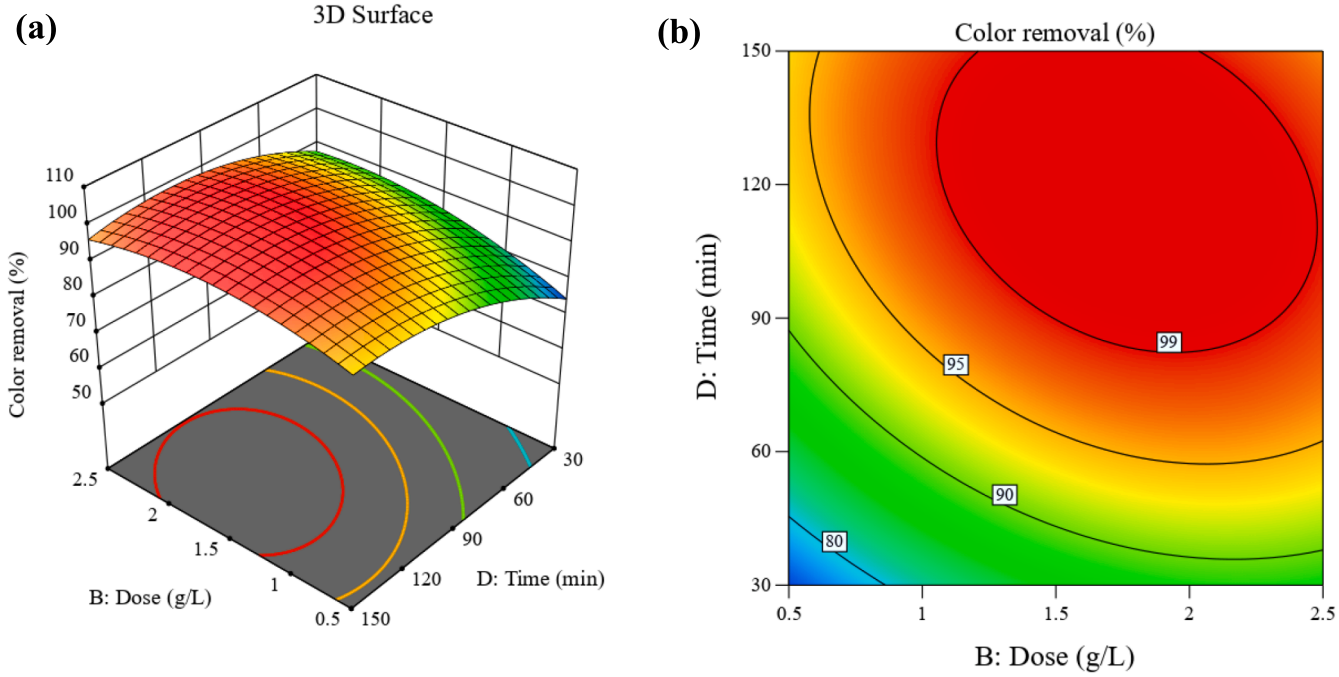

Fig. 15. Effect catalyst dose and reaction time:(a) 3D surface plot and (b) contour plot.

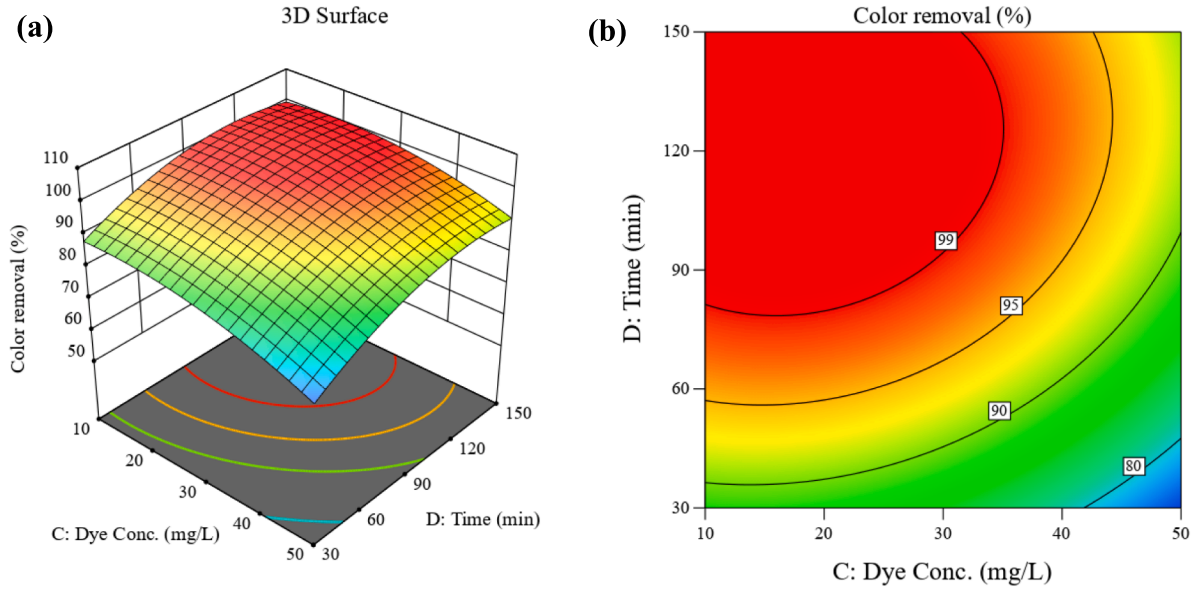

Fig. 16. Effect of initial dye concentration and reaction time: (a) 3D surface plot and (b) contour.

3.7.6. *Initial dye concentration and irradiation time*

Fig. 16 illustrates the interaction between initial dye concentration and reaction time on BB41 removal, demonstrating a significant correlation through three-dimensional response surface and contour plots derived from RSM analysis. This study explored initial dye concentrations ranging from 10 to 50 mg/L and irradiation times between 30 and 150 min using a constant pH of 7 and a catalyst dose of 1.5 mg/L. The highest degradation efficiency (99 %) was achieved at dye concentrations of 10–33 mg/L with irradiation times of 85–120 min, whereas the lowest efficiency was observed at 50 mg/L with an irradiation time of just 30 min. As the dye concentration decreased from 32 to 10 mg/L, the irradiation time was reduced from 120 to 85 min, while still maintaining the same high efficiency. These results suggest that higher dye concentrations demand longer reaction times for optimal degradation. Adjusting both dye concentration and irradiation time enhances control over the photocatalytic process, enabling efficient dye removal without excessive catalyst use, while sustaining high degradation efficiency across different concentration levels.

3.8. *Numerical parameter optimization*

Optimization of BB41 dye degradation efficiency was performed using numerical methods through Design-Expert-13 software. Different parameters, including pH (3–11), catalyst dose (0.5–2.5 g/L), initial dye concentration (10–50 mg/L), and reaction time (30–150 min), were varied within their defined ranges. The color removal responses were set at a maximum level with a 95 % confidence level. The desirability function approach was implemented to determine the optimized conditions. From a total of 100 solution sets, the most desirable (99.5 %) and optimal condition was selected. As shown in Fig. 17, the optimal

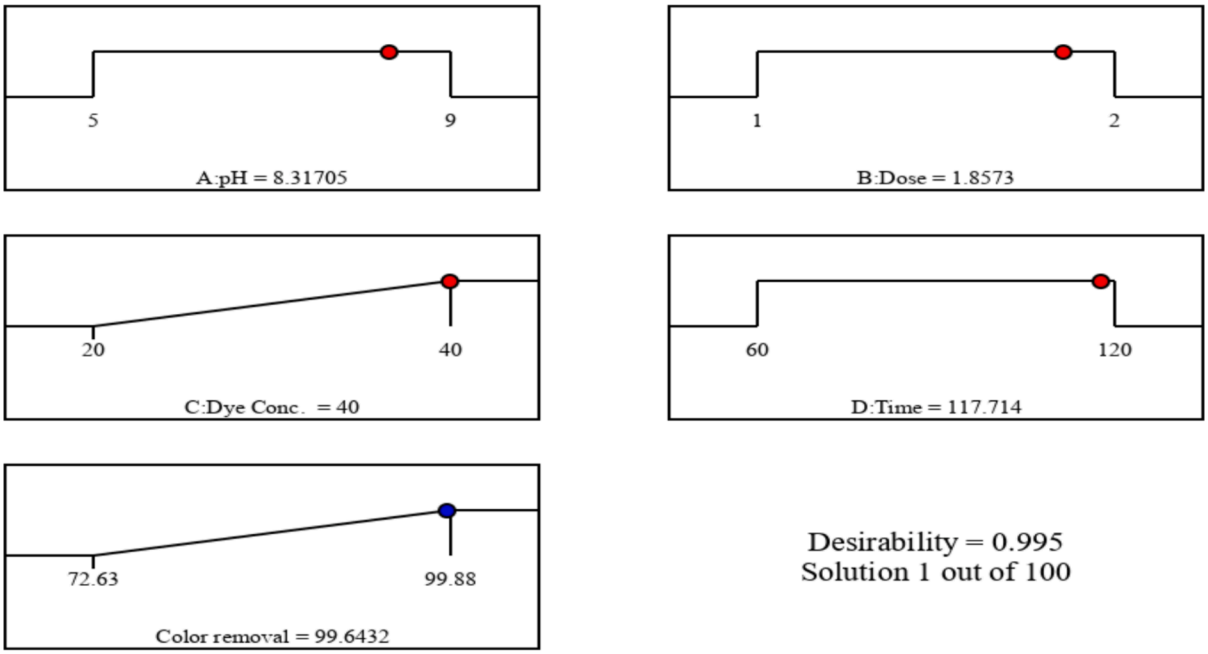

Fig. 17. Ramp plot.

conditions for the photocatalytic removal of BB41 were determined to be a pH of 8.3, a catalyst load of 1.85 g, an initial dye concentration of 40 mg/L, and a reaction time of 118 min. Under these conditions, a color removal efficiency of 99.6 % was achieved. Experimental verification of the optimized conditions demonstrated less than a 1 % deviation from the predicted results, confirming the accuracy and effectiveness of the optimization approach. This validation highlights the model's reliability in predicting optimal parameters for maximum degradation efficiency, further supporting its use in practical applications. Moreover, achieving a mineralization efficiency of 92.8 % showcases how effective the catalyst is, making it both precise and cost-effective for water treatment. Previous studies have also pointed out how economical and reliable Response Surface Methodology (RSM) is for optimizing experiments. This aligns with previous studies that have highlighted the economic viability of Response Surface Methodology (RSM) for experimental optimizations due to its predictability and precision [43,100]. Table 6 provides a summary of the photocatalytic degradation efficiency of TiO_2-based composite catalysts for removing Basic Blue 41 (BB41) dye under various conditions. The photodegradation efficiency of the TiO_2-BC (TBC-2) composite was further evaluated through triplicate experiments, targeting the removal of BB41 dye, color, turbidity, and chemical oxygen demand (COD) from actual textile effluent. The initial concentrations in the textile effluent were 5.7 mg/L for BB41 dye, 106pt-Co for color, 48.55 NTU for turbidity, and 928 mg/L for COD. The corresponding removal efficiencies were approximately 94.8 % for BB41 dye, 96.2 % for color, 89.28 % for turbidity, and 66.6 %for COD. While the color, turbidity, and BB41 dye concentrations were effectively removed, the treated wastewater still contained approximately 309.9 mg/L of COD. Although this level is close to meeting the IPA standard minimum threshold of 250 mg/L, further treatment is necessary to reduce the COD level even more. Another study conducted on textile BB41 dye-containing effluent treated with AC-TiO_2 composite resulted in a color and turbidity removal of 96.5 % and 92.9 % respectively [43]. This study further supports the idea that the TiO_2-BC composite can effectively remove hazardous color pollutants from textile wastewater.

3.9. Photocatalytic degradation mechanism

The photocatalytic degradation of Basic Blue 41 (BB41) dye using TBC-2 composites reveals significant insights into the mechanisms of pollutant degradation, particularly the roles of hydroxyl radicals (·OH), holes (h^+), and superoxide radicals. As shown in Fig. 18a the experimental results indicate that the presence of scavengers, such as sodium oxalate, n-butanol, and ascorbic acid, reduced the degradation efficiency of BB41, showing the critical involvement of all oxidizing species. Specifically, the degradation efficiencies were 99.5 % without scavengers, dropping to 60.2 %, 76.1 %, and 67.7 % with n-butanol, ascorbic acid, and sodium oxalate, respectively. This suggests that hydroxyl radicals are the primary reactive species, while holes contribute as secondary reactive species. Superoxide also contributes significantly to dye degradation in photocatalytic systems. The findings show the importance of optimizing photocatalytic conditions to maximize the generation of these reactive species for effective wastewater treatment. Hydroxyl radicals, as highly reactive oxidizing agents, are essential in breaking down organic compounds, By targeting the conjugated structures that give the dye its color. Their ability to generate a cascade of oxidation reactions ensures rapid and efficient pollutant breakdown, making them the primary species driving the photodegradation process. Holes, also play a critical role in dye degradation. Research indicates that holes can account for up to 60 % of dye degradation in photocatalytic systems [101]. Their strong oxidative potential enables them to directly interact with dye molecules, oxidizing chemical bonds and leading to decolorization and mineralization. This capability makes holes highly effective in degrading complex dye structures during environmental remediation. In conclusion, the active species driving BB41 dye degradation are primarily hydroxyl radicals (·OH) and holes (h+) with hydroxyl radicals serving as the dominant contributors. Fig. 18b presents the proposed degradation mechanism for BB41, further elucidating the critical roles of these reactive species.

Table 6
Evaluation of the photocatalytic degradation efficiency of BB41 dye using various catalysts.

No	Catalysts	Condition	Degradation	references
1	AC-25 %TiO_2	BB41 [dye] = 2.5 M, catalyst dose = 0.25/100 mL, pH = 6, and time 45 min. under UV light	95 %	[43]
2	*Cm*-ZnO NPs	BB41 [dye] = 20 mg/L, catalyst dose = 5 g/L, pH = 10 time = 60 min under UV light	97.69 %	[102]
3	NiO nanoparticles	BB41 [dye] = 20 mg/L, catalyst dose 5 g/L, pH = 10 time = 50 min under UV light	93.6 %	[103]
4	ZnO	BB41 [dye] = 20 mg/L, catalyst dose 2 g/L, pH = 5, time = 180 min under UV light	72.56 %	[104]
5	TiO_2-ZnO	BB41 [dye] = 20 mg/L, catalyst dose 10 g/L, pH = 6.2. time = 60 min under solar light	100 %	[105]
6	TiO_2-20 wt% BC(TBC-2)	BB41 [dye] = 40 mg/L, catalyst dose 1.8 g/L, pH = 8.2 time = 120 min under UV light	99.6 %	This study

3.10. Photodegradation kinetics and photocatalytic reusability

Kinetic studies were performed to assess the photocatalytic degradation rates of BB41 under optimal conditions: pH 8.3, a catalyst dose of 1.85 g/L, an initial dye concentration of 40 mg/L, and an irradiation duration of 118 min. The degradation process was analyzed using zero-order, first-order, and second-order kinetic models, with the results illustrated in Fig. 19 (a–c) and Table 7. The adjusted R^2 values were 0.475, 0.992, and 0.544, respectively. These findings indicate that the degradation of BB41 using the TiO_2-BC composite aligns closely with the first-order kinetic model, suggesting that the reaction rate is directly proportional to the concentration of the dye being degraded. The reaction rate constant (k) was calculated as 0.049 min^{-1}, further confirming the consistency of the first-order kinetic model. The high R^2 value demonstrates the model's accuracy in describing the degradation behavior over time. Comparatively, another study also reported the degradation of BB41 dye using bare TiO_2 and AC/TiO_2 composite (AC-TiO_2). The degradation followed a first-order kinetics model with rate constants of 0.0322 min^{-1} for TiO_2 and 0.0366 min^{-1} for AC-TiO_2 [43]. The higher rate constant of 0.049 min^{-1} observed in this study highlights the efficiency of the TiO_2-BC composite, indicating faster photocatalytic degradation of BB41 under the specified conditions. Fig. 19d shows the recycling performance of the TiO_2-biochar (TBC-2) composite under optimal conditions. The results indicate that the composite initially maintained high degradation efficiency. After four recycling cycles, a slight reduction in efficiency was observed. Over five cycles, the degradation efficiency decreased from 99.6 % to 96.3 %, a minimal reduction of 3.32 %. This demonstrates that the TiO2-BC composite retains excellent photodegradation performance and remains highly effective in degrading BB41 dye. Additionally, the recycling process does not require extra treatment, underscoring the composite's potential as a practical and sustainable solution for water treatment applications.

4. Conclusions

In summary, the TiO_2-biochar composite photocatalyst was

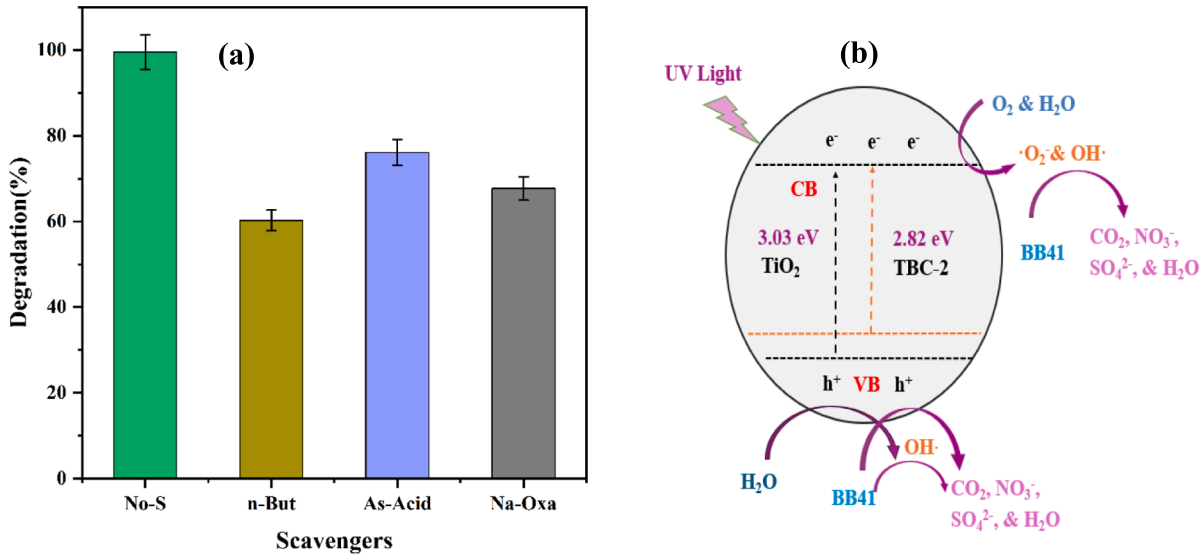

Fig. 18. (a) Scavenger test results for BB41 dye degradation and (b) Schematic representation of the photodegradation mechanism of BB41 dye via TBC-2 photocatalysis.

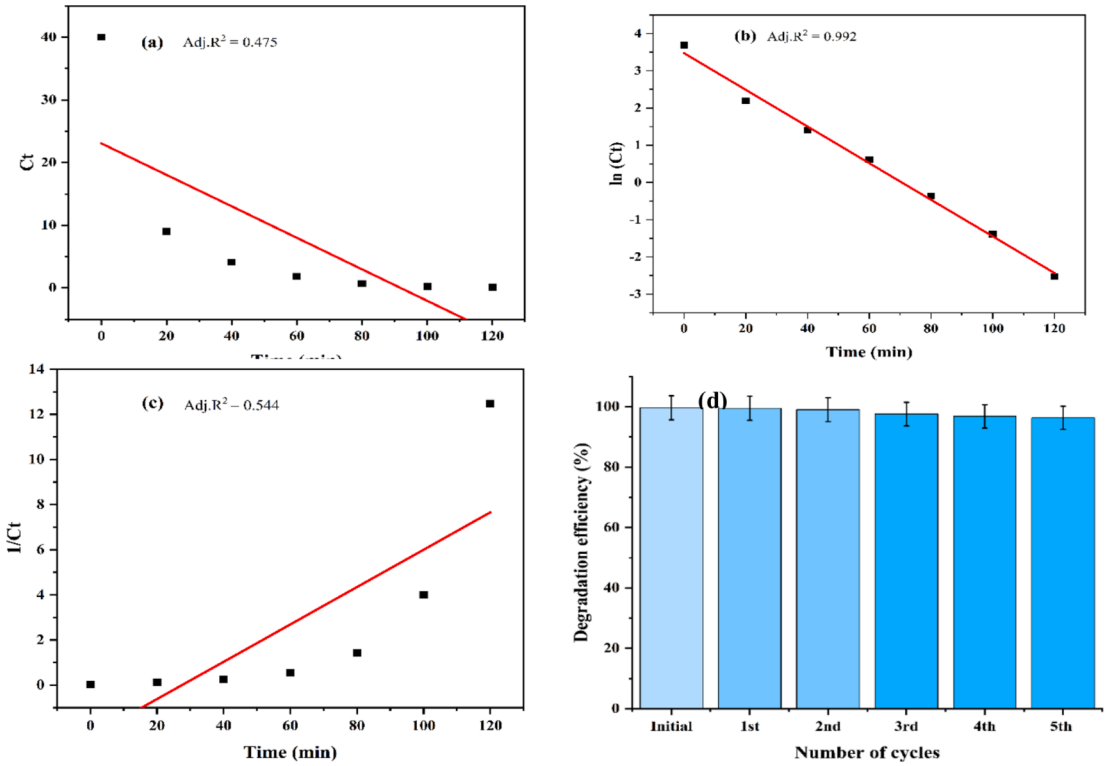

Fig. 19. (a) Zero-order kinetic,(b) First-order kinetic, and (c)Second-order kinetic model analysis of BB41 dye degradation. (d) Recycling performance of the TiO_2-BC composite for BB41 dye removal under optimized conditions.

successfully synthesized via the Sol-Gel method at 600 °C, resulting in a material with an anatase crystal structure, a reduced bandgap of 2.82 eV, and a significantly increased surface area from 38 m^2/g to 118.89 m^2/g. The photocatalytic efficiency was optimized using Response Surface Methodology (RSM) with a Central Composite Design under UV light irradiation. Statistical analysis through ANOVA confirmed the model's high significance for color removal ($p < 0.05$) with an R^2 value of 0.99. The composite achieved a maximum photodegradation efficiency of 99.6 % for BB41 dye removal under optimal conditions: pH 8.3, an initial dye concentration of 40 mg/L, a catalyst dosage of 1.85 g/L, and an irradiation time of 117 min, with a desirability score of 99.5 %. Furthermore, it demonstrated exceptional removal efficiencies of 99.6 % for BB41 dye in aqueous solutions and 94.8 % for textile wastewater, along with a 66.6 %reduction in COD. The degradation kinetics followed a first-order model with a rate constant of $k = 0.049\ min^{-1}$. The TiO_2-biochar composite also exhibited remarkable reusability, maintaining high efficiency over five recycling cycles with only a 3.32 % reduction in performance. These findings highlight the potential of the TiO_2-biochar composite as an economical, sustainable, and efficient solution for large-scale wastewater treatment and the removal of dye contaminants from

Table 7
Photodegradation kinetics model values .

Kinetics model	Intercept	Slope	k_0, (mg/L.min)	k_1 (min^{-1})	k_2 (L/(mg. min))	Adj. R^2
Zero-order kinetics	23.08	−0.25	0.25	–	–	0.475
1st order kinetics	3.47	−0.049	–	0.049	–	0.992
2nd order kinetics	−2.27	0.082	–	–	0.082	0.544

aqueous systems.

Consent to participate

Not applicable.

Consent to publish

Not applicable.

Ethical approval

Not applicable.

CRediT authorship contribution statement

Mohammednur Abdu: Writing – review & editing, Writing – original draft, Software, Resources, Methodology, Investigation, Funding acquisition, Formal analysis, Data curation, Conceptualization. **Saeideh Babaee:** Writing – review & editing, Writing – original draft, Visualization, Validation. **Abebe Worku:** Writing – review & editing, Writing – original draft, Visualization, Validation, Supervision, Resources, Project administration. **Palesa Diale:** Writing – review & editing, Writing – original draft, Visualization, Validation, Supervision. **Titus A.M. Msagati:** Writing – review & editing, Writing – original draft, Visualization, Validation, Supervision, Data curation. **Jemal Fito Nure:** Writing – review & editing, Writing – original draft, Visualization, Validation, Supervision, Resources, Project administration, Investigation, Funding acquisition, Formal analysis, Data curation, Conceptualization.

Funding

The research did not receive specific funding but was performed as part of the Addis Ababa Science and Technology University. No fund was received for the manuscript writing and editing approval.

Declaration of competing interest

The authors declare that they have no known competing financial interests or personal relationships that could have appeared to influence the work reported in this paper.

Acknowledgments

We would like to thank the University of South Africa, College of Science, Engineering, and Technology University for financial support and other facilities, and we would like to thank the School of Chemical and Metallurgical Engineering, University of the Witwatersrand, 1 Jorissen St, Johannesburg 2000, South Africa.

Authors contributions

MA, JFN, and AW contributed to concept development, experimental design, experimental statistical analysis, and manuscript writing and editing. Research data were collected by HA. Then, JFN MT and AW supervision, and fund acquisition. MA, JFN, PD, AW, SB, and MA statistical analysis, manuscript writing, editing, and data validation.

Compliance with ethical standards

Not applicable.

Data availability

All the data is included in the manuscript.

References

[1] A. Arif, M. Malik, S. Liaqat, A. Aslam, K. Mumtaz, A. Afzal, D. Ch, K. Nisa, F. Khurshid, F. Arif, M. Shah, Z. Khalid, R. Javed, M. Khalid, Water pollution and industries, Pure Appl. Biol. 9 (4) (2020) 2214–2224, https://doi.org/10.19045/bspab.2020.90237.
[2] S. Ahmed, S. Ismail, Water pollution and its sources, effects & management: a case study of Delhi, Int. J. Curr. Adv. Res. 7 (2) (2018) 10436–10442.
[3] M.B.K. Suhan, S.B. Shuchi, M.R. Al-Mamun, H. Roy, M.S. Islam, Enhanced UV light-driven photocatalytic degradation of methyl orange using MoO3/WO3-fluorinated TiO2 nanocomposites, Environ. Nanotechnol. Monit. Manage. 19 (2023) 100768, https://doi.org/10.1016/j.enmm.2022.100768.
[4] T.U. Rahman, H. Roy, A.Z. Shoronika, A. Fariha, M. Hasan, M.S. Islam, H. M. Marwani, A. Islam, M.M. Hasan, A.K.D. Alsukaibi, M.M. Rahman, M.R. Awual, Sustainable toxic dye removal and degradation from wastewater using novel chitosan-modified TiO2 and ZnO nanocomposites, J. Mol. Liq. 388 (2023) 122764, https://doi.org/10.1016/j.molliq.2023.122764.
[5] M.B.K. Suhan, M.R. Al-Mamun, N. Farzana, S.M. Aishee, M.S. Islam, H. M. Marwani, M.M. Hasan, A.M. Asiri, M.M. Rahman, A. Islam, M.R. Awual, Sustainable pollutant removal and wastewater remediation using TiO2-based nanocomposites: a critical review, Nano-Struct. Nano-Objects 36 (2023) 101050, https://doi.org/10.1016/j.nanoso.2023.101050.
[6] J. Liu, Y. Zhang, L. Deng, Citric acid-assisted preparation of BiOCOOH-TiO2 composite photocatalyst for efficient degradation of Rhodamine B, Inorg. Chem. Commun. (2025) 113946, https://doi.org/10.1016/j.inoche.2025.113946.
[7] M.L. Serejo, M.F. Morgado, D. García, A. González-Sánchez, H.O. Méndez-Acosta, A. Toledo-Cervantes, Environmental resilience by microalgae, in: Microalgae Cultivation for Biofuels Production, Elsevier, 2020, pp. 293–315.
[8] H. Roy, T.U. Rahman, M.A.J.R. Khan, M.R. Al-Mamun, S.Z. Islam, M.A. Khaleque, M.I. Hossain, M.Z.H. Khan, M.S. Islam, H.M. Marwani, A. Islam, M.M. Hasan, M. R. Awual, Toxic dye removal, remediation, and mechanism with doped SnO2-based nanocomposite photocatalysts: a critical review, J. Water Process Eng. 54 (2023) 104069, https://doi.org/10.1016/j.jwpe.2023.104069.
[9] M.R. Al-Mamun, S. Kader, M.S. Islam, Solar-TiO2 immobilized photocatalytic reactors performance assessment in the degradation of methyl orange dye in aqueous solution, Environ. Nanotechnol. Monit. Manage. 16 (2021) 100514, https://doi.org/10.1016/j.enmm.2021.100514.
[10] J. Cui, F. Zhang, H. Li, J. Cui, Y. Ren, X. Yu, Recent progress in biochar-based photocatalysts for wastewater treatment: synthesis, mechanisms, and applications, Appl. Sci. 10 (3) (2020) 1019.
[11] S. Kittappa, F.M. Jais, M. Ramalingam, N.S. Mohd, S. Ibrahim, Functionalized magnetic mesoporous palm shell activated carbon for enhanced removal of azo dyes, J. Environ. Chem. Eng. 8 (5) (2020) 104081.
[12] R. Mansour, Natural dyes and pigments: extraction and applications, J. Renew. Mater. Color. Finishing (2018) 75–102.
[13] L. Hamdi, L. Boumehdi, Z. Salem, Basic blue 41 dye removal from aqueous solution using lignocellulosic material: kinetics, equilibrium and statistical design optimization, Int. J. Environ. Sci. Technol. 20 (3) (2023) 3275–3294, https://doi.org/10.1007/s13762-022-04188-7.
[14] D.A. Yaseen, M. Scholz, Textile dye wastewater characteristics and constituents of synthetic effluents: a critical review, Int. J. Environ. Sci. Technol. 16 (2) (2019) 1193–1226.
[15] L.R. Buddiga, B.B.V. Sailaja, G. Rao Gajula, S.R. Nayak, An investigation on characterizations and application of Cu-TiO2/WO3 nanocomposite for degradation of indigo carmine dye, Inorg. Chem. Commun. 156 (2023) 111171, https://doi.org/10.1016/j.inoche.2023.111171.
[16] C. Yao, M. Wang, W. Jiang, Y. Chen, Study on a novel N-doped mesoporous carbon for the efficient removal of methylene blue from aqueous solution, Environ. Eng. Res. 26 (5) (2021).
[17] M. Rashid Al-Mamun, K.T. Hossain, S. Mondal, M. Afroza Khatun, M. Shahinoor Islam, Z.H. Khan, Synthesis, characterization, and photocatalytic performance of methyl orange in aqueous TiO2 suspension under UV and solar light irradiation, S. Afr. J. Chem. Eng. 40 (2022) 113–125, https://doi.org/10.1016/j.sajce.2022.02.002.
[18] S. Kader, M.R. Al-Mamun, M.B.K. Suhan, S.B. Shuchi, M.S. Islam, Enhanced photodegradation of methyl orange dye under UV irradiation using MoO3 and Ag doped TiO2 photocatalysts, Environ. Technol. Innov. 27 (2022) 102476, https://doi.org/10.1016/j.eti.2022.102476.
[19] K.V. Plakas, A. Taxintari, A.J. Karabelas, Enhanced photo-catalytic performance of activated carbon fibers for water treatment, Water 11 (9) (2019) 1794.

[20] A.A. Aziz, S. Ibrahim, Preparation of activated carbon/N-doped titania composite for synergistic adsorption-photocatalytic oxidation of batik dye, IOP Conf. Ser.: Mater. Sci. Eng. 358 (1) (2018) 12014.
[21] G. Divya, G. Jaishree, T. Sivarao, K.V.D. Lakshmi, Microwave assisted sol–gel approach for Zr doped TiO2 as a benign photocatalyst for bismark brown red dye pollutant, RSC Adv. 13 (13) (2023) 8692–8705, https://doi.org/10.1039/D3RA00328K.
[22] V. Uthiravel, K. Narayanamurthi, V. Raja, S. Anandhabasker, K. Kuppusamy, Green synthesis and characterization of TiO2 and Ag-doped TiO2 nanoparticles for photocatalytic and antimicrobial applications, Inorg. Chem. Commun. 170 (2024) 113327, https://doi.org/10.1016/j.inoche.2024.113327.
[23] A. Khlyustova, N. Sirotkin, T. Kusova, A. Kraev, V. Titov, A. Agafonov, Doped TiO2: the effect of doping elements on photocatalytic activity, Mater. Adv. 1 (5) (2020) 1193–1201.
[24] J. Zhou, B. Zhu, L. Wang, Y. Li, Q. Qiao, Enhanced photocatalytic activity of Fe-doped TiO2 coated on N-doped activated carbon composites for photocatalytic degradation of dyeing wastewater, AIP Conf. Proc. 1890 (1) (2017) 20009.
[25] S. Chandra, P. Jagdale, I. Medha, A.K. Tiwari, M. Bartoli, A.D. Nino, F. Olivito, Biochar-supported TiO2-based nanocomposites for the photocatalytic degradation of sulfamethoxazole in water—a review, Toxics 9 (11) (2021), https://doi.org/10.3390/toxics9110313.
[26] Y. Koo, G. Littlejohn, B. Collins, Y. Yun, V.N. Shanov, M. Schulz, D. Pai, J. Sankar, Synthesis and characterization of Ag–TiO2–CNT nanoparticle composites with high photocatalytic activity under artificial light, Compos. B Eng. 57 (2014) 105–111.
[27] N. Kadiyala, T. Siva Rao, D. Gorli, S. Sai Supriya, S. Vidavalur, Raffiunnisa, Fabrication of dual phased heterojunction Vanadium-Boron codoped nanoTiO2 composite: Twin applications in dye degradation and antimicrobial activity, Inorg. Chem. Commun. 162 (2024) 112240, https://doi.org/10.1016/j.inoche.2024.112240.
[28] M.A.M. Adnan, N.M. Julkapli, M.N.I. Amir, A. Maamor, Effect on different TiO_2 photocatalyst supports on photodecolorization of synthetic dyes: a review, Int. J. Environ. Sci. Technol. 16 (1) (2019) 547–566.
[29] T. Fazal, A. Razzaq, F. Javed, A. Hafeez, N. Rashid, U.S. Amjad, M.S.U. Rehman, A. Faisal, F. Rehman, Integrating adsorption and photocatalysis: a cost effective strategy for textile wastewater treatment using hybrid biochar-TiO2 composite, J. Hazard. Mater. 390 (2020) 121623.
[30] X. Xiong, K.M. Iris, L. Cao, D.C.W. Tsang, S. Zhang, Y.S. Ok, A review of biochar-based catalysts for chemical synthesis, biofuel production, and pollution control, Bioresour. Technol. 246 (2017) 254–270.
[31] W. Wang, J. Zhang, T. Chen, J. Sun, X. Ma, Y. Wang, J. Wang, Z. Xie, Preparation of TiO2-modified biochar and its characteristics of photo-catalysis degradation for enrofloxacin, Sci. Rep. 10 (1) (2020) 1–12.
[32] J. Fito, K.K. Kefeni, T.T.I. Nkambule, The potential of biochar-photocatalytic nanocomposites for removal of organic micropollutants from wastewater, Sci. Total Environ. 829 (2022) 154648, https://doi.org/10.1016/j.scitotenv.2022.154648.
[33] W.-J. Liu, H. Jiang, H.-Q. Yu, Development of biochar-based functional materials: toward a sustainable platform carbon material, Chem. Rev. 115 (22) (2015) 12251–12285.
[34] S. Zhang, X. Lu, Treatment of wastewater containing Reactive Brilliant Blue KN-R using TiO2/BC composite as heterogeneous photocatalyst and adsorbent, Chemosphere 206 (2018) 777–783.
[35] S. Silvestri, M.G. Goncalves, P.A. da Silva Veiga, T.T. da Silva Matos, P. Peralta-Zamora, A.S. Mangrich, TiO2 supported on Salvinia molesta biochar for heterogeneous photocatalytic degradation of Acid Orange 7 dye, J. Environ. Chem. Eng. 7 (1) (2019) 102879.
[36] H. Zhang, Z. Wang, R. Li, J. Guo, Y. Li, J. Zhu, X. Xie, TiO2 supported on reed straw biochar as an adsorptive and photocatalytic composite for the efficient degradation of sulfamethoxazole in aqueous matrices, Chemosphere 185 (2017) 351–360.
[37] X. Cai, J. Li, Y. Liu, Z. Yan, X. Tan, S. Liu, G. Zeng, Y. Gu, X. Hu, L. Jiang, Titanium dioxide-coated biochar composites as adsorptive and photocatalytic degradation materials for the removal of aqueous organic pollutants, J. Chem. Technol. Biotechnol. 93 (3) (2018) 783–791.
[38] J.R. Kim, E. Kan, Heterogeneous photocatalytic degradation of sulfamethoxazole in water using a biochar-supported TiO2 photocatalyst, J. Environ. Manag. 180 (2016) 94–101.
[39] B. Wang, B. Liu, X.-X. Ji, M.-G. Ma, Synthesis, characterization, and photocatalytic properties of bamboo charcoal/TiO2 composites using four sizes powder, Materials (Basel) 11 (5) (2018) 670.
[40] L. Lu, R. Shan, Y. Shi, S. Wang, H. Yuan, Chemosphere A novel TiO2/biochar composite catalysts for photocatalytic degradation of methyl orange, Chemosphere 222 (2019) 391–398, https://doi.org/10.1016/j.chemosphere.2019.01.132.
[41] A.S. El-Shafie, M. Abouseada, M. El-Azazy, TiO2-functionalized biochar from pistachio nutshells: adsorptive removal and photocatalytic decolorization of methyl orange, Appl. Water Sci. 13 (12) (2023) 227, https://doi.org/10.1007/s13201-023-02035-9.
[42] M. Abdu, S. Babaee, A. Worku, T.A.M. Msagati, J.F. Nure, The development of Giant reed biochar for adsorption of Basic Blue 41 and Eriochrome Black T. azo dyes from wastewater, Sci. Rep. 14 (1) (2024) 18320, https://doi.org/10.1038/s41598-024-67997-5.
[43] E. Kweinor Tetteh, E. Obotey Ezugbe, D. Asante-Sackey, E.K. Armah, S. Rathilal, Response surface methodology: photocatalytic degradation kinetics of Basic Blue 41 dye using activated carbon with TiO2, Molecules 26 (4) (2021), https://doi.org/10.3390/molecules26041068.
[44] S. Hmamouchi, A. El Yacoubi, M. El Hezzat, B. Sallek, B.C. El Idrissi, Optimization of photocatalytic parameters for MB degradation by g-C3N4 nanoparticles using Response Surface Methodology (RSM), Diam. Relat. Mater. 136 (2023) 109986, https://doi.org/10.1016/j.diamond.2023.109986.
[45] M. Hasanpour, S. Motahari, D. Jing, M. Hatami, Statistical analysis and optimization of photodegradation efficiency of methyl orange from aqueous solution using cellulose/zinc oxide hybrid aerogel by response surface methodology (RSM), Arab. J. Chem. 14 (11) (2021) 103401, https://doi.org/10.1016/j.arabjc.2021.103401.
[46] S.J.S. Chelladurai, K. Murugan, A.P. Ray, M. Upadhyaya, V. Narasimharaj, S. Gnanasekaran, Optimization of process parameters using response surface methodology: a review, Mater. Today Proc. 37 (2021) 1301–1304.
[47] M. Kifetew, E. Alemayehu, J. Fito, Z. Worku, S.V. Prabhu, B. Lennartz, Adsorptive removal of reactive yellow 145 dye from textile industry effluent using teff straw activated carbon: optimization using central composite design, Water 15 (7) (2023), https://doi.org/10.3390/w15071281.
[48] M. Abdu, S. Tibebu, S. Babaee, A. Worku, T.A.M. Msagati, J.F. Nure, Optimization of photocatalytic degradation of eriochrome black T from aqueous solution using TiO2-biochar composite, Results Eng. (2025) 104036, https://doi.org/10.1016/j.rineng.2025.104036.
[49] H. Elbushra, M. Ahmed, H. Wardi, N. Eassa, Synthesis and characterization of TiO2 using sol-gel method at different annealing temperatures, MRS Adv. 3 (42–43) (2018) 2527–2535, https://doi.org/10.1557/adv.2018.230.
[50] Y. Jiang, A. Liu, Cornstalk biochar-TiO2 composites as alternative photocatalyst for degrading methyl orange, Environ. Sci. Pollut. Res. 30 (11) (2023) 31923–31934.
[51] T. Mahmood, M.T. Saddique, A. Naeem, P. Westerhoff, S. Mustafa, A. Alum, Comparison of different methods for the point of zero charge determination of NiO, Ind. Eng. Chem. Res. 50 (17) (2011) 10017–10023, https://doi.org/10.1021/ie200271d.
[52] N. Rosly, A. Abdullah, M. Ahmad Kamarudin, E. Ashari, S. Ahmad, Adsorption of methylene blue dye by calix[6]arene-modified lead sulphide (Pbs): optimisation using response surface methodology, Int. J. Environ. Res. Public Health 18 (2021) 397, https://doi.org/10.3390/ijerph18020397.
[53] B. Mondol, A. Sarker, A.M. Shareque, S.C. Dey, M.T. Islam, A.K. Das, S. M. Shamsuddin, M.A.I. Molla, M. Sarker, Preparation of activated carbon/TiO2 nanohybrids for photodegradation of reactive red-35 dye using sunlight, Photochem 1 (1) (2021) 54–66.
[54] A. Moges, T.T.I. Nkambule, J. Fito, The application of GO-Fe 3 O 4 nanocomposite for chromium adsorption from tannery industry wastewater, J. Environ. Manage. 305 (2022) 114369, https://doi.org/10.1016/j.jenvman.2021.114369.
[55] D. Bedada, K. Angassa, A. Tiruneh, H. Kloos, J. Fito, Chromium removal from tannery wastewater through activated carbon produced from Parthenium hysterophorus weed, Energy Ecol. Environ. 5 (3) (2020) 184–195, https://doi.org/10.1007/s40974-020-00160-8.
[56] J.F. Nure, A. Mengistu, M. Abewaa, K. Angassa, W. Moyo, Z. Phiri, P.J. Mafa, A. T. Kuvarega, T.T.I. Nkambule, Adsorption of Black MNN reactive dye from tannery wastewater using activated carbon of Rumex abysinicus, J. Taiwan Inst. Chem. Eng. 151 (2023) 105138.
[57] N. Abu Bakar, N. Othman, Z.M. Yunus, Z. Daud, N. Salsabila Norisman, M. Haziq Hisham, Physico-chemical water quality parameters analysis on textile, IOP Conf. Ser.: Earth Environ. Sci 498 (1) (2020) 12077, https://doi.org/10.1088/1755-1315/498/1/012077.
[58] A. Panhwar, K. Faryal, A. Kandhro, S. Bhutto, U. Rashid, N. Jalbani, R. Sultana, A. Solangi, M. Ahmed, S. Qaisar, Z. Solangi, M. Gorar, E. Sargani, Utilization of treated industrial wastewater and accumulation of heavy metals in soil and okra vegetable, Environ. Challenges 6 (2022) 100447, https://doi.org/10.1016/j.envc.2022.100447.
[59] T.T. Wondim, R.B. Dzwairo, D. Aklog, E. Janka, G. Samarakoon, M.M. Dereseh, Wastewater treatment plant performance assessment using time-function-based effluent quality index and multiple regression models: the case of Bahir Dar textile factory, Environ. Monit. Assess. 195 (11) (2023) 1360, https://doi.org/10.1007/s10661-023-11952-w.
[60] E. Al-Oubidy, F. Kadhim, Photocatalytic activity of anatase titanium dioxide nanostructures prepared by reactive magnetron sputtering technique, Opt. Quant. Electron. 51 (2019), https://doi.org/10.1007/s11082-018-1738-z.
[61] A.G. Adeniyi, J.O. Ighalo, D.V. Onifade, Production of biochar from elephant grass (Pernisetum purpureum) using an updraft biomass gasifier with retort heating, Biofuels (2019) 1–8, https://doi.org/10.1080/17597269.2019.1613751.
[62] R. Wu, W. Liu, R. Bai, D. Zheng, X. Tian, W. Lin, Q. Ke, L. Li, Waste biomass-mediated synthesis of TiO2/P, K-containing grapefruit peel biochar composites with enhanced photocatalytic activity, Molecules 29 (9) (2024) 2090.
[63] J. Wang, T. Yu, M. Wang, X. Guo, Y. Chen, A novel biochar-composed TiO2 (BC-Ti) for efficient photocatalytic degradation on arbidol, J. Ind. Eng. Chem. 134 (2024) 537–547.
[64] M.-A. Gatou, A. Syrrakou, N. Lagopati, E.A. Pavlatou, Photocatalytic TiO2-based nanostructures as a promising material for diverse environmental applications: a review, Reactions 5 (1) (2024) 135–194.
[65] A. Kowalczyk, B. Zgardzińska, K. Osipiuk, K. Jędruchniewicz, K.T. Rotko, M. Goździuk, H. Wang, B. Czech, The visible-light-driven activity of biochar - doped TiO2 photocatalysts in β-blockers removal from water, Materials (Basel) (2023).

[66] J. Song, M. Shi, L. Xia, J. Dai, L. Luo, H. Wang, L. Shu, F. Jiang, The comparative study on inhibitory effect of natural organic matters on the TiO2 and activated carbon/TiO2 composites for the removal of 17α-ethinylestradiol, Chemosphere 333 (2023) 138930, https://doi.org/10.1016/j.chemosphere.2023.138930.
[67] S. Samangsri, T.A.S. Chiarakorn, of methylene blue dye, Res. Chem. Intermed. 49 (4) (2023) 1649–1664, https://doi.org/10.1007/s11164-022-04925-0.
[68] B. Xing, C. Shi, C. Zhang, G. Yi, L. Chen, H. Guo, G. Huang, J. Cao, Preparation of TiO2/activated carbon composites for photocatalytic degradation of RhB under UV light irradiation, J. Nanomater. 2016 (2016).
[69] L. Kanku, K.O. Badmus, F. Wewers, Biochar-supported titanium oxide for the photocatalytic treatment of orange II sodium salt, Appl. Nano 5 (3) (2024) 190–204, https://doi.org/10.3390/applnano5030013.
[70] Y. Liu, X. Dai, J. Li, S. Cheng, J. Zhang, Y. Ma, Recent progress in TiO 2–biochar-based photocatalysts for water contaminants treatment: strategies to improve photocatalytic performance, RSC Adv. 14 (1) (2024) 478–491.
[71] K.R. Gustavsen, T. Feng, H. Huang, G. Li, U. Narkiewicz, K. Wang, DFT calculation of carbon-doped TiO2 nanocomposites, Materials 16 (18) (2023), https://doi.org/10.3390/ma16186117.
[72] P. Lisowski, J.C. Colmenares, O. Mašek, Dual functionality of TiO2/biochar hybrid materials: photocatalytic phenol degradation in liquid phase and selective oxidation of methanol in gas phase, ACS Sustain. Chem. Eng. (2017).
[73] E. Dervishi, Z. Ji, H. Htoon, M. Sykora, S.K. Doorn, Raman spectroscopy of bottom-up synthesized graphene quantum dots: size and structure dependence, Nanoscale 11 (35) (2019) 16571–16581, https://doi.org/10.1039/C9NR05345J.
[74] Y. Yan, S. Manickam, E. Lester, T. Wu, C.H. Pang, Synthesis of graphene oxide and graphene quantum dots from miscanthus via ultrasound-assisted mechano-chemical cracking method, Ultrason. Sonochem. 73 (2021), https://doi.org/10.1016/j.ultsonch.2021.105519.
[75] A.C. Martins, A.L. Cazetta, O. Pezoti, J.R.B. Souza, T. Zhang, E.J. Pilau, T. Asefa, V.C. Almeida, Sol-gel synthesis of new TiO2/activated carbon photocatalyst and its application for degradation of tetracycline, Ceram. Int. 43 (5) (2017) 4411–4418.
[76] J. Liu, L. Zheng, Y. Gao, L. Ji, Z. Yang, H. Wang, M. Shang, J. Du, X. Yang, TiO2/p-BC composite photocatalyst for efficient removal of tetracycline from aqueous solutions under simulated sunlight, Catalysts 14 (6) (2024), https://doi.org/10.3390/catal14060357.
[77] A.K. Singh, D.A. Giannakoudakis, M. Arkas, K.S. Triantafyllidis, V. Nair, Composites of lignin-based biochar with BiOCl for photocatalytic water treatment: RSM studies for process optimization, Nanomaterials 13 (4) (2023), https://doi.org/10.3390/nano13040735.
[78] A.K. Inamdar, S.A. Inamdar, C.T. Birajdar, J. Bhale, S.V. Rajmane, B.H. Shinde, S. P. Patole, S.B. Shelke, S.N. Inamdar, Applications of titanium dioxide (TiO2) nanoparticles in photocatalysis, Sci. Adv. Mater. 16 (7) (2024) 757–771.
[79] Y. Wei, H. Meng, Q. Wu, X. Bai, Y. Zhang, TiO2-based photocatalytic building material for air purification in sustainable and low-carbon cities: a review, Catalysts 13 (12) (2023) 1466.
[80] K. Jedynak, B. Charmas, Adsorption properties of biochars obtained by KOH activation, Adsorption (2023), https://doi.org/10.1007/s10450-023-00399-7.
[81] M. Zeng, Influence of TiO2 surface properties on water pollution treatment and photocatalytic activity influence of TiO2 surface properties on water pollution treatment and photocatalytic activity, Bull. Kor. Chem. Soc. (2015), https://doi.org/10.5012/bkcs.2013.34.3.953.
[82] M. An, Z. Yang, B. Zhang, B. Xue, G. Xu, W. Chen, S. Wang, Construction of biochar-modified TiO2 anatase-rutile phase S-scheme heterojunction for enhanced performance of photocatalytic degradation and photocatalytic hydrogen evolution, J. Environ. Chem. Eng. 11 (5) (2023) 110367.
[83] M.S. Mohtaram, S. Mohtaram, S. Sabbaghi, X. You, W. Wu, L. Jia, K. Muzammil, N.A. Alraee, S. Islam, Y. Aryanfar, Photocatalytic degradation of acetaminophen using a novel TiO2-orange peel-derived biochar composite: synthesize, characterization and optimization of key factors, J. Water Process Eng. 58 (2024) 104884.
[84] S. Hmamouchi, Y. Abbad, A. El Yacoubi, A. Boulouiz, B. Sallek, B.C. El Idrissi, Optimization study of methylene blue dye adsorption on Chamaerops humilis fibers biosorption using a central composite design, Desalin. Water Treat. 320 (2024) 100824, https://doi.org/10.1016/j.dwt.2024.100824.
[85] H. Roy, T.R. Prantika, M.H. Riyad, S. Paul, M.S. Islam, Synthesis, characterizations, and RSM analysis of Citrus macroptera peel derived biochar for textile dye treatment, S. Afr. J. Chem. Eng. 41 (2022) 129–139, https://doi.org/10.1016/j.sajce.2022.05.008.
[86] H. Roy, M.S. Islam, M.T. Arifin, S.H. Firoz, Synthesis, characterization and sorption properties of biochar, chitosan and ZnO-based binary composites towards a cationic dye, Sustainability 14 (21) (2022), https://doi.org/10.3390/su142114571.
[87] H. Roy, M.S. Islam, M.T. Arifin, S.H. Firoz, Chitosan-ZnO decorated Moringa oleifera seed biochar for sequestration of methylene blue: isotherms, kinetics, and response surface analysis, Environ. Nanotechnol. Monit. Manage. 18 (2022) 100752, https://doi.org/10.1016/j.enmm.2022.100752.
[88] P. Gharbani, A. Mehrizad, S.A. Mosavi, Optimization, kinetics and thermodynamics studies for photocatalytic degradation of Methylene Blue using cadmium selenide nanoparticles, npj Clean Water 5 (1) (2022) 34, https://doi.org/10.1038/s41545-022-00178-x.
[89] S. Yildiz, S. Kaya, G.T. Canbaz, M.M. Maslov, Elucidating the mechanisms of AV17 and BB41 dye degradation through combined computational and applied analyses, J. Mol. Struct. 1308 (2024) 138054, https://doi.org/10.1016/j.molstruc.2024.138054.
[90] A. Ajmal, I. Majeed, R.N. Malik, H. Idriss, M.A. Nadeem, Principles and mechanisms of photocatalytic dye degradation on TiO2 based photocatalysts: a comparative overview, RSC Adv. 4 (70) (2014) 37003–37026.
[91] M.E. Kounaris Fuziki, L.S. Ribas, A.M. Tusset, R. Brackmann, O.A.A. Dos Santos, G.G. Lenzi, Pharmaceutical compounds photolysis: pH influence, Heliyon 9 (2) (2023) e13678, https://doi.org/10.1016/j.heliyon.2023.e13678.
[92] K.M. Reza, A.S.W. Kurny, F. Gulshan, Parameters affecting the photocatalytic degradation of dyes using TiO2: a review, Appl. Water Sci. 7 (2017) 1569–1578.
[93] A. Zuorro, R. Lavecchia, M.M. Monaco, G. Iervolino, V. Vaiano, Photocatalytic degradation of azo dye reactive violet 5 on Fe-doped titania catalysts under visible light irradiation, Catalysts 9 (8) (2019) 645.
[94] S.M. Fouad, Y.M.S. El-Shazly, M.A. Alyoubi, S.A. Nosier, M.H. Abdel-Aziz, Enhanced photocatalytic degradation of cationic dyes using slurry of anatase titania in a falling film reactor, Case Stud. Chem. Environ. Eng. 8 (2023) 100518, https://doi.org/10.1016/j.cscee.2023.100518.
[95] P. Akhter, F. Ali, A. Ali, M. Hussain, TiO2 decorated CNTs nanocomposite for efficient photocatalytic degradation of methylene blue, Diam. Relat. Mater. 141 (2024) 110702, https://doi.org/10.1016/j.diamond.2023.110702.
[96] N. Desch, A. Rheindorf, C. Fassbender, M. Sloot, M. Lake, Photocatalytic degradation of methylene blue by anatase TiO2 coating, Appl. Res. (2023) e202300081.
[97] S.M. Anisuzzaman, C.G. Joseph, C.K. Pang, N.A. Affandi, S.N. Maruja, V. Vijayan, Current trends in the utilization of photolysis and photocatalysis treatment processes for the remediation of dye wastewater: a short review, ChemEngineering 6 (4) (2022), https://doi.org/10.3390/chemengineering6040058.
[98] M.-J. Tsai, M.-Y. Chung, M.-Y. Kuo, J.-Y. Wu, Effective enhancement of performances on photo-assisted dye degradation using a Zn coordination polymer and its post-modified Cu/Zn bimetallic analogue under natural environments, J. Environ. Chem. Eng. 11 (2) (2023) 109258.
[99] M.Z. Alam, M.N. Bari, S. Kawsari, Statistical optimization of Methylene Blue dye removal from a synthetic textile wastewater using indigenous adsorbents, Environ. Sustain. Indic. 14 (2022) 100176.
[100] S. Mortazavian, A. Saber, D.E. James, Optimization of photocatalytic degradation of acid blue 113 and acid red 88 textile dyes in a UV-C/TiO2 suspension system: application of response surface methodology (RSM), Catalysts 9 (4) (2019) 360.
[101] L. Kuang, Y. Zhao, W. Zhang, S. Ge, Roles of reactive oxygen species and holes in the photodegradation of cationic and anionic dyes by TiO 2 under UV irradiation, J. Environ. Eng. 142 (2) (2016) 4015065.
[102] M. Sivagami, D. Thirumalai, I.V. Asharani, Photocatalytic degradation of toxic basic blue 41 and reactive orange M2R dyes using green synthesized zinc oxide nanoparticles, J. Indian Chem. Soc. 101 (10) (2024) 101326, https://doi.org/10.1016/j.jics.2024.101326.
[103] M. Sivagami, D. Thirumalai, P.V.S. Narayana, A. Murugeeswari, I.V. Asharani, Enhanced photocatalytic activity of BB41 and ROM2R dyes using green synthesized NiO nanoparticles: a response surface methodology approach, J. Taiwan Inst. Chem. Eng. 165 (2024) 105816, https://doi.org/10.1016/j.jtice.2024.105816.
[104] N.M. Mahmoodi, S. Keshavarzi, M. Ghezelbash, Synthesis of nanoparticle and modelling of its photocatalytic dye degradation ability from colored wastewater, J. Environ. Chem. Eng. 5 (4) (2017) 3684–3689, https://doi.org/10.1016/j.jece.2017.07.010.
[105] Y. Jiang, Y. Sun, H. Liu, F. Zhu, H. Yin, Solar photocatalytic decolorization of C.I. Basic Blue 41 in an aqueous suspension of TiO2–ZnO, Dyes Pigm. 78 (1) (2008) 77–83, https://doi.org/10.1016/j.dyepig.2007.10.009.